# A Three-Dimensional Particle Tracking Velocimetry System for the Evaluation of Large Eddy Simulation Turbulence Models

Joshua M. Hunt

A thesis submitted in partial fulfillment of the
requirements for the degree of

Master of Science

University of Washington

2016

Committee:

Dana Dabiri, Chair

James Riley

Program Authorized to Offer Degree:
Aeronautics and Astronautics

University of Washington

## Abstract

A Three-Dimensional Particle Tracking
Velocimetry System for the Evaluation of Large-Eddy
Simulation Turbulence Models

Joshua Hunt

Chair of the Supervisory Committee:
Associate Professor Dana Dabiri
Aeronautics and Astronautics

The necessity for evaluating the accuracy and characteristics of new Large-Eddy Simulation (LES) turbulence models in modern fluid mechanics research has inspired the development of a Three-Dimensional Particle Tracking Velocimetry (3DPTV) system capable of producing 3-Dimension 3-Component (3D3C) velocity vector fields. The system is based on the triangulation method of particle location and utilizes an optical system comprised of three 4008 x 2672 charge-coupled devices (CCDs), three 120mm lenses, and a water-filled prism. The tracer particles used in the system were $<5\mu$m $TiO_2$ and were illuminated using a 532 nm Nd:YAG dual pulsed laser. The system was configured to study a backward-facing step flow in a 6" x 12" water tunnel due to this flow's consistency in separation and unsteady, turbulent characteristics. The experimental flow had a freestream velocity of 22 cm/s, a Reynolds number based on the step height of 6274, and a Taylor-microscale Reynolds number of approximately 130. Data from this flow was used in *a priori* testing of various LES models including the Smagorinsky, Similarity, Mixed, Dynamic, Coherent Structures, and Stretched Vortex Models. The system is preferable to Direct Numerical Simulation (DNS) for such testing in that it is capable of acquiring data at a resolution adequate for *a priori* testing without the computational restrictions for high Reynolds numbers. In the present configuration, the system is capable of achieving a Taylor-microscale Reynolds number of 214, but with an increase to the CCD resolution of the system, a Taylor-microscale Reynolds number of nearly 400 would be attainable.

The views expressed are those of the author and do not reflect the official policy or position of the US Air Force, Department of Defense or the US Government

# TABLE OF CONTENTS

Page

List of Figures. . . . . iv

List of Tables. . . . . vi

Glossary. . . . . vii

Chapter 1: Introduction. . . . . 1

1.1 Backward-Facing Step Flow. . . . . 2

1.1.1 Separated Shear Layer. . . . . 3

1.1.2 Recirculating and Reattachment Regions. . . . . 4

Chapter 2: Turbulence Modeling and Theory. . . . . 6

2.1 Direct Numerical Simulation. . . . . 6

2.2 Reynolds-Averaged Navier Stokes. . . . . 7

2.2.1 The Turbulent Viscosity Hypothesis. . . . . 8

2.3 Large-Eddy Simulation. . . . . 9

2.3.1 Subgrid-Scale Models. . . . . 11

2.3.2 Smagorinsky Model. . . . . 12

2.3.3 Similarity Model. . . . . 13

2.3.4 Mixed Models. . . . . 14

2.3.5 Dynamic Models. . . . . 15

2.3.6 Dynamic Mixed Models. . . . . 17

2.3.7 Coherent Structures Model. . . . . 17

2.3.8 Stretched Vortex Model. . . . . 19

Chapter 3: Experimental Setup and Methodology. . . . . 21
3.1 Historical Experimental Approaches. . . . . 21
3.1.1 Two-Dimensional PDV. . . . . 22
3.1.2 Three-Dimensional Holographic PIV. . . . . 24
3.1.3 Argument for a 3DPTV Method. . . . . 25
3.2 The Design of a 3DPTV System for Evaluating LES Models. . . . . 25
3.3 Flow Facility. . . . . 30
3.3.1 Test Section and Flow Settings. . . . . 30
3.3.2 Volume of Interest. . . . . 32
3.3.3 Particle Siphon System. . . . . 33
3.4 Optical/Camera System. . . . . 34
3.4.1 Charge-Coupled Devices (CCDs) . . . . . 35
3.4.2 Lenses. . . . . 36
3.4.3 Water-Filled Prism. . . . . 36
3.5 Illumination Source. . . . . 38
3.5.1 Solo PIV Laser. . . . . 38
3.5.2 Laser Sheet Optics. . . . . 40
3.6 Calibration Equipment and Procedure. . . . . 40
3.6.1 Grid Dot Pattern Target. . . . . 40
3.6.2 Calibration Rigs. . . . . 42
3.6.3 Calibration Illumination. . . . . 44
3.6.4 Calibration Procedure. . . . . 45
3.7 Data Acquisition and Experimental Procedure. . . . . 48
3.7.1 Data Acquisition System Architecture. . . . . 48
3.7.2 Laser Illumination, Alignment, and Timing. . . . . 49
3.7.3 Particle Selection and Seeding. . . . . 50
3.7.4 Experimental Procedure. . . . . 51

Chapter 4: Results and Discussion. . . . . 53
4.1 3DPTV Results. . . . . 53
4.2 Evaluation of SGS Stress Models. . . . . 56
4.2.1 SGS Stress Contours and Correlations. . . . . 57
4.2.2 SGS Dissipation Contours and Correlations. . . . . 60
4.2.3 SGS Force Correlation. . . . . 63
4.3 Uncertainty Analysis. . . . . 64
4.3.1 Uncertainty of the Velocity. . . . . 64
4.3.2 Uncertainty of the Filtered Velocity. . . . . 66
4.3.3 Uncertainty of the Various LES Models. . . . . 67
4.4 Improving the Present 3DPTV System. . . . . 72
4.4.1 Methods of Increasing Reynolds Number.. . . . . 73
4.4.2 Implications of Increasing Reynolds Number. . . . . 73
4.4.3 CCD Resolution Study. . . . . 75
4.4.4 Improving Vector Density. . . . . 78

Chapter 5: Conclusions and Future Study. . . . . 80
5.1 Conclusions. . . . . 80
5.2 Future Study. . . . . 82
5.2.1 Increased CCD Resolution for Increased Reynolds Number. . . . . 82
5.2.2 Removable Lens System for Increasing Resolution. . . . . 82
5.2.3 Smaller Particles for Increased Vector Density. . . . . 83
5.2.4 Re-evaluation of the Calibration Method. . . . . 83
5.2.5 Re-evaluation of the Camera Setup. . . . . 84
5.2.6 Additional Evaluation of Stretched Vortex Model.. . . . . 85

5.2.7 Further Recommendations from Dona. . . . . 85
5.2.8 Ranking of Future Studies. . . . . 86

# LIST OF FIGURES


1.1 Backward-facing step flow regions. . . . . 2

1.2 Backward-facing step flow recirculation region regions. . . . . 4

3.1 3DPTV System Schematic regions. . . . . 26

3.2 3DPTV imaged volume defined in *X*-*Z* plane regions. . . . . 27

3.3 Three-dimensional view of imaging volume regions. . . . . 27

3.4 3DPTV Design Parameters. . . . . 28

3.5 Flow Facility. . . . . 30

3.6 Water tunnel test section. . . . . 31

3.7 Approximate location of VOI. . . . . 32

3.8 Particle Siphon/Seeding System. . . . . 34

3.9 CCDs and mounts. . . . . 35

3.10 Lens cross section. . . . . 36

3.11 Astigmatism caused by refraction in air, acrylic, and water. . . . . 37

3.12 Ray tracing showing effect of water-filled prism. . . . . 37

3.13 Water-filled prism. . . . . 38

3.14 Laser sheet formation. . . . . 39

3.15 Halo illumination of particles. . . . . 40

3.16 Calibration plate dimensions. . . . . 41

3.17 Calibration rig with fixed rods. . . . . 43

3.18 False tunnel top and calibration rig. . . . . 44

3.19 Calibration illumination scheme. . . . . 45

3.20 Distortion patterns from camera misalignment. . . . . 46

3.21 Data acquisition equipment control diagram. . . . . 48

3.22 Laser and camera timing diagram. . . . . 50

3.23 Particle seeding diagram. . . . . 51
4.1 3DPTV 3D3C vector field. . . . . 54
4.2 3DPTV structured results. . . . . 55
4.3 Contours of mean vorticity. . . . . 55
4.4 Experimental SGS stress contours. . . . . 57
4.5 LES SGS stress contours. . . . . 58
4.6 Experimental SGS energy dissipation. . . . . 60
4.7 LES SGS energy dissipation. . . . . 61
4.8 Uncertainty of filtered rate of strain. . . . . 68
4.9 Uncertainty of the Smagorinsky Model. . . . . 69
4.10 Uncertainty of the Similarity Model. . . . . 71
4.11 Uncertainty of the Mixed Model. . . . . 72
4.12 Map of multiphase coupling regions. . . . . 77
4.13 Particle images in Dona (2014) . . . . . 79
4.14 Particle images in present study. . . . . 79
5.1 Example configuration for new 3DPTV system. . . . . 85

# LIST OF TABLES


4.1 LES model SGS stress correlation coefficients. . . . . 59

4.2 LES model SGS energy dissipation correlation. . . . . 63

4.3 LES model SGS force correlation. . . . . 63

4.4 Resolvable scales for various CCD resolutions. . . . . 76

# GLOSSARY

3DPTV: Three-Dimensional Particle Tracking Velocimetry

LES: Large-Eddy Simulation

SGS: Sub-Grid Scale

DNS: Direct Numerical Simulation

RANS: Reynolds-Averaged Navier-Stokes

PIV: Particle Image Velocimetry

PDV: Particle Displacement Velocimetry

HPIV: Holographic Particle Image Velocimetry

DDPIV: Digital Defocused Particle Image Velocimetry

3D3C: Three-Dimensional Three-Component

CCD: Charge-Coupled Device

VOI: Volume of Interest

RTM: Ray Tracing Matrix

RBF: Radial Basis Function

DVR: Digital Video Recorder

SVD: Singular Value Decomposition

CSM: Coherent Structures Model

SVM: Stretched Vortex Model

# ACKNOWLEDGEMENTS

I would first like to thank the University of Washington Department of Aeronautics and Astronautics for giving me the opportunity to engage in such a rich and rewarding program. I would furthermore like to thank Professor Dana Dabiri not only for his support and guidance, but also for letting me be a part of such a complex research project. His confidence in my ability to tackle the project was valuable motivation. I especially thank Lieutenant Nick Dona for all of his help and patience orienting me to the project. I would also like to express gratitude to Professor James Riley for serving on the advisory committee and providing insight for the future of this work. Thank you also to Ed Connery, Professor Gamal Khalil, Lieutenant Lilly Pryor, and Lieutenant Trey Cottingham for the guidance and mentorship. I would also like to thank the U.S. Air Force for providing me the opportunity to pursue this degree and the U.S. Air Force Academy's Department of Aeronautics for giving me the tools necessary for its pursuit. Finally, thank you Mom and Dad for the constant love and support and thank you Zach, Abby, and Katie for doing what you do. And of course, thank you to the boys of 6549 53rd Ave NE for the laughs along the way.

# Chapter 1

# INTRODUCTION

To the scientist, engineer, or physicist, turbulence is not merely the unsettling bumps an airline passenger experiences as he crosses the Rocky Mountains on his flight from New York to Los Angeles. While this often distressing and uncomfortable situation is certainly related to fluid turbulence, it is but a side-effect of a far more complex and rich phenomenon. The chaotic, disorganized flow is ever present. It shows up in the back eddies of rivers, the exhaust of a car, the crashing of a wave, and even the smoke coming from the pipe of an old fluid mechanics professor. Not only is this flow ever present, but, at least according to famous theoretical physicist Richard Feynman, "[t]urbulence is the most important unsolved problem of classical physics."[1]

While the importance of its study is undeniable and well-documented, turbulence remains one of the most difficult phenomena to study. The non-linearity and complexity of the governing Navier-Stokes Equations continues to perplex mathematicians and to date, there is no analytical solution to the equations. For this reason, engineers must solve these equations numerically, an approach that leads to prohibitive computational costs as the flow gets increasingly more complex. However, one promising way to study turbulence is to gather experimental data for a consistently turbulent flow and compare the experimental data to turbulence models designed to estimate certain terms in the Navier-Stokes Equations. A three-dimensional particle tracking velocimetry (3DPTV) system has been developed at the University of Washington to do this.

The system's design, implementation, resulting data as well as the theory and application of Large-Eddy Simulation (LES) models to this experimental data is the subject of this study.

### 1.1 Backward-Facing Step Flow

The specific turbulent flow selected to be studied by this system was a backward facing step flow. The following section describes, in brief, the characteristics of this flow.

Backward-facing step flow is a popular flow phenomenon to study as it provides consistent flow separation and unsteady behaviors characteristic of turbulence.[2] Its unsteady behavior and consistent point of separation provide an abundance of flow phenomenon to study. Backward-facing step flow consists of several major regions including the inflow, a separated shear layer, a recirculation region, and a reattachment point.[3] A schematic of the regions in backward-facing step flow can be seen in Figure 1.1 below. These regions will be described in further detail in the following sections.

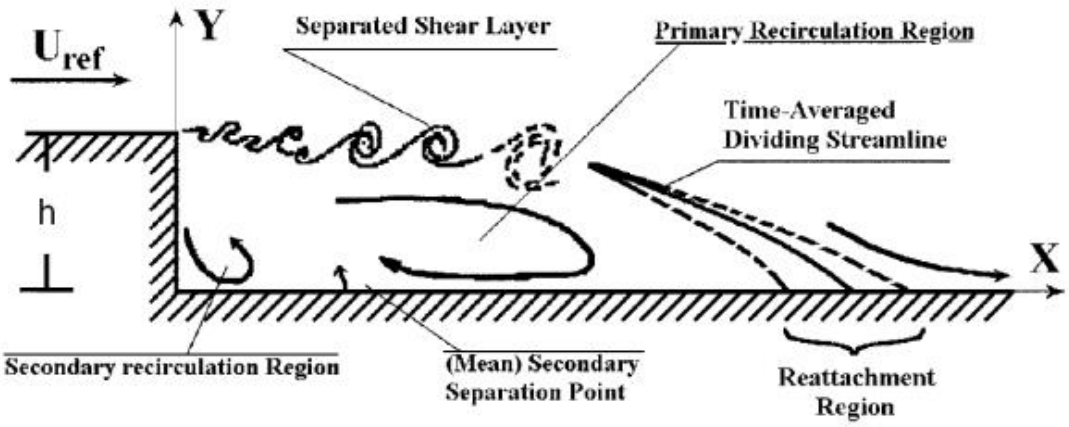


Figure 1.1: Backward-facing step flow regions[3]

*1.1.1 Separated Shear Layer*

As the inflow in backward-facing step flow passes over the physical step, a separated shear layer forms. Initially, this flow is comprised of the boundary-layer that forms at the top of the step, but as the flow crosses the step, distinct separation of this boundary-layer occurs. Just beyond the distinct separation point, the flow becomes analogous to free shear flow.[3] More specifically, this free shear flow regions is a plane mixing layer, which is a region of turbulent flow that forms between two parallel flows of different velocities.[4] Troutt *et al.* have experimentally shown that the span-wise vorticity structures throughout this separated shear layer are similar to those of a mixing free shear layer.[5] Furthermore, observation of backward-facing step flow shows that this separated shear layer region favors the lower-velocity region thus causing the net flow to bend downward toward the tunnel floor.

While the separated shear layer is similar to a plane mixing layer, it is important to note that there is a key difference. Specifically, the shear layer portion of this flow is spatially limited. That is, since it is close in proximity to the reattachment region seen in Figure 1.1, the shear layer does not have the opportunity to become fully developed. Additionally, this shear layer is a vortex sheet that results from the velocity discontinuity at the separation point. This vortex sheet rolls up, experiences the Kelvin-Helmholtz instability, and results in vortex shedding.[2,3] Significant experimental investigation has been conducted by Scarano *et al.* to characterize the unsteady behavior of the individual vortex structures in the vortex sheet that exists in this region.[6]

The incredibly unsteady behavior of this region of backward-facing step flow makes Large-Eddy Simulation (LES) of sub-grid scale (SGS) stresses complex. Popular LES models such as the Dynamic Smagorinsky Model, which will be described in later sections, rely on

averaging coefficients along a direction of statistical homogeneity.[7] This clearly poses a difficulty for non-homogeneous flows such as the flow studied here. To address this problem, a number of new models have been proposed to implement dynamic models for complex statistically non-homogeneous flows. These are promising models which highlight the potential for significant innovation in the field of LES modeling and require test and evaluation on a variety of flow phenomenon. For this reason, the present study focuses on testing these models using high resolution experimental data. These models, and the methods used for testing, will be described in subsequent sections.

### *1.1.2 Recirculating and Reattachment Regions*

As seen in Figure 1.1, beyond the separated shear-layer region of the backward-facing step flow, the flow begins to recirculate and reattach. A significant portion of the research conducted on backward-facing step flow has been spent evaluating the mean flow behind the step. The goal of this research is typically to establish a mean location for where the reattachment region is located, $X_r$, seen in Figure 1.2.

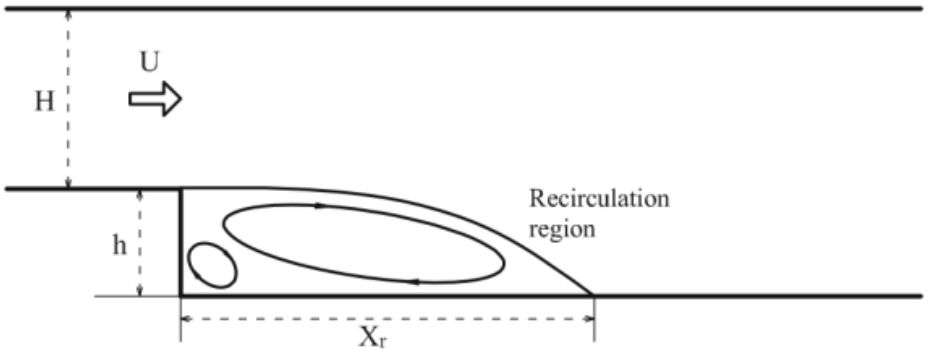


Figure 1.2: Backward-facing step flow recirculation region[3]

Experiments conducted by Armaly (1983) and Barri (2010) have investigated the location of the reattachment region for a variety of step heights and Reynolds numbers based on this height, $Re_h$, as defined in Equation 1.1.[8,9]

$$Re_h = \frac{\rho u_{in} h}{\mu}. \tag{1.1}$$

In this formulation $h$ represents the step height, $u_{in}$ is the freestream velocity, $\rho$ is the fluid density, and $\mu$ is the fluid viscosity. Another parameter experimenters have investigated in backward facing step flow has been the location of this reattachment region with respect to the ratio of the post-step channel height to the inflow height, known as the channel expansion ratio, ER.[10] The equation for this expansion ratio can be seen in Equation 1.2 below where $H$ and $h$ are the channel height prior to the step and step height respectively, as seen in Figure 1.2.

$$ER = \frac{H+h}{H}. \tag{1.2}$$

It is also worth noting that some LES modeling has been used to study the recirculation region. Specifically, Kobayashi *et al*. (1992) used the Smagorinsky Model to resolve the physics of the eddies in the recirculation region in an attempt to determine the location of the reattachment location. In this study however, the Smagorinsky Model likely resulted in an insignificant amount of turbulence, which likely resulted in an overestimation of the step-normalized reattachment length, $X_r/h$ of between 9 and 10.[3,11] In addition to the recirculation region, this reattachment point has been closely studied. This location is important as it dictates the streamwise location at which the boundary layer becomes highly turbulent.

# Chapter 2

## TURBULENCE MODELING AND THEORY

In the following chapter, a brief description of turbulence modeling to include Direct Numerical Simulation (DNS), Reynolds-Averaged Navier-Stokes (RANS), and Large-Eddy Simulation (LES) modeling is presented. The main focus of the present study was 3DPTV's application to LES turbulence modeling. For this reason, the review is focused on the LES models investigated.

### 2.1 Direct Numerical Simulation

While the present study focuses on using experimental Three Dimensional Particle Tracking Velocimetry (3DPTV), which will be described in subsequent sections, to evaluate turbulence models for backward-facing step flow, it is important to understand the significance of turbulence and LES modeling from a theoretical perspective. In Direct Numerical Simulation, the governing incompressible momentum equation, shown in Equation 2.1. This equation is part of the overall governing Navier-Stokes Equations and is solved iteratively on a finite spatial grid at one instance in time in DNS.

$$\frac{\partial \boldsymbol{u}}{\partial t} + \boldsymbol{u} \cdot \boldsymbol{\nabla u} = -\frac{\nabla P}{\rho} + \nu \nabla^2 \boldsymbol{u} \qquad (2.1)$$

In this equation, $\boldsymbol{u}$ represents the three dimensional velocity vector, $P$ is the pressure, $\nu$ is the kinematic viscosity of the fluid being studied, $\rho$ is its density, and $t$ is time. In the past, DNS has been unfeasible due to the high computational time required to achieve results at an adequately high resolution to study turbulence. However, with the development of high-speed computing,

this method is becoming more feasible and is attractive due to its relative simplicity and accuracy of results at the scales resolved.

It is clear DNS has several key benefits, but it is also important to note that DNS reflects only one instance of the flow field being resolved. If a researcher wants to resolve more than one instance of the flow, and thus get a time history of how the flow field develops, the computational cost rises dramatically. The computational time also increases significantly when more complex, higher Reynolds number flows are studied. In fact, according to Pope (2000), the number of days required to complete a DNS simulation roughly scales with $(Re_L/800)^3$. For more information on how this relation was developed, see Pope (2000).[4] This indicates that a flow with a relatively modest Reynolds number of 10,000 would take nearly 2000 days, or almost 5.5 years, to adequately resolve the turbulent scales of the flow. While this estimation is based on a maximum computing rate of 1 gigaflop and today's most powerful computers are capable of processing at nearly 350 gigaflops, it is important to see that DNS becomes increasingly prohibitive as Reynolds number increases.[3] Such a prohibitive trend with increasing Reynolds number has led researchers to take alternative approaches to studying turbulence. Two important, less computationally expensive methods are the Reynolds-Averaged Navier-Stokes (RANS) method, and Large-Eddy Simulation (LES).

### 2.2 Reynolds-Averaged Navier-Stokes

One method for reducing the computational time associated with directly solving the Navier-Stokes equations is to solve the time-averaged Navier-Stokes equations, this approach is called the Reynolds-Averaged Navier-Stokes (RANS) method. Derivation of the RANS equations begins with the Reynolds decomposition which says that the velocity vector, $\boldsymbol{u}$, can be

decomposed into a time-averaged component, $\langle \boldsymbol{u} \rangle$, and a fluctuating component, $\boldsymbol{u}'$. In this decomposition, and henceforth, the bracket symbol, $\langle\ \rangle$, indicates time-averaging as defined by $\langle \boldsymbol{u} \rangle = \int_0^T \boldsymbol{u} dt$ where *t* is time and *T* is some characteristic time. The Reynolds decomposition of the velocity is then input for the velocity term in Equation 2.1, the momentum equation of the Navier-Stokes Equation. The process of substituting the Reynolds decomposition in for the velocity, simplifying, and grouping terms results in the RANS equations seen in Equation 2.2 below.[4] Note that for simplicity, these equations are presented in Einstein notation.

$$\rho \frac{\bar{D}\langle u_j \rangle}{\bar{D}t} = \frac{\partial}{\partial x_i}\left[\mu\left(\frac{\partial \langle u_i \rangle}{\partial x_j} + \frac{\partial \langle u_j \rangle}{\partial x_i}\right) - \langle p \rangle \delta_{ij} - \rho \langle u'_i u'_j \rangle\right]. \tag{2.2}$$

Solutions to this equation involve the mean velocity field since the original equations are time averaged. Furthermore, these solutions require a model for the Reynolds stresses, $\langle u'_i u'_j \rangle$, to provide closure to the problem. Many of these models involve obtaining the Reynolds stresses through turbulent-viscosity models. The details of these models can be seen in Pope (2000).[4]

### *2.2.1 The Turbulent-Viscosity Hypothesis*

An important RANS model for turbulence analysis is known as the turbulent-viscosity hypothesis. Note that this turbulent-viscosity is sometimes referred to as eddy-viscosity. This hypothesis relies on an intrinsic and a specific assumption to model the Reynolds stress.[4] First, the intrinsic assumption is that at each point in time, the Reynolds stress anisotropy, $a_{ij} \equiv \langle u'_i u'_j \rangle - \frac{2}{3} k \delta_{ij}$, is given by the mean velocity gradients, $\frac{\partial \langle u_i \rangle}{\partial x_j}$. The specific assumption then is that the relationship between the Reynolds stress anisotropy, also known as the deviatoric portion, and the mean velocity gradients is given by Equation 2.3.[4]

$$a_{ij} \equiv \langle u'_i u'_j \rangle - \frac{2}{3} k \delta_{ij} = -\nu_T \left(\frac{\partial \langle u_i \rangle}{\partial x_j} - \frac{\partial \langle u_j \rangle}{\partial x_i}\right) = -2\nu_T \bar{S}_{ij}, \tag{2.3}$$

where $\bar{S}_{ij}$ is the mean rate of strain tensor. This then leads to the Reynolds stresses being modeled by Equation 2.4 below.

$$\langle u'_i u'_j \rangle = \frac{2}{3} k \delta_{ij} - 2\nu_T \bar{S}_{ij} \tag{2.4}$$

This equation now provides closure to the RANS equations presented in Equation 2.2, but the turbulent, or eddy, viscosity, $\nu_T$, remains to be specified. This term is given by the product of a length and a velocity, meaning that the task of modeling $\nu_T$ is generally left to specifying this length and velocity.

### 2.3 Large-Eddy Simulation

Perhaps the most popular and growing facet of turbulence research is in Large-Eddy Simulation (LES). LES is unique in that it uses a DNS approach for the larger scale motions and models the small-scale motions. Since the high computational cost of DNS lies in resolving the fine-scale motions, modeling these motions through LES significantly decreases computational time. In a way, LES attempts to alleviate the shortcomings of both DNS and RANS. It is much less computationally expensive than DNS, but is able to model unsteadiness in the flow that RANS is unable to capture.[4]

LES can be somewhat complex, but ultimately there are only four conceptual steps in the LES process. First, a filtering step, as originally proposed by Leonard (1974) is performed. This filtering step decomposes the velocity field ***u(x,t)*** into the sum of a filtered, $\tilde{\boldsymbol{u}}$**(x,**t), and a residual component ***u'(x,t).*** This residual component is also known as the subgrid-scale, SGS component. The filtered velocity is three-dimensional, time-dependent, and represents the motion of the larger eddies.[4,12] The equation for the filtered velocity can be seen in Equation 2.5.

$$\tilde{\boldsymbol{u}}(\boldsymbol{x}, t) = \int G_{\Delta}(\boldsymbol{r}, \boldsymbol{x}) \boldsymbol{u}(\boldsymbol{x} - \boldsymbol{r}, t) d\boldsymbol{r}. \tag{2.5}$$

In this equation, ***G(r,x),*** is the filtering kernel, by which the velocity field is convolved at each fine-scale location, ***x***. This yields the filtered velocity field with an LES grid spacing Δ. A common filter used in this convolution kernel is a simple Gaussian, $G_{\Delta}^{Gaus}(\boldsymbol{x})$. This LES filter is a function of the LES grid spacing Δ. The standard LES Gaussian filter, as seen in Pope, has a variance of $\sigma^2 = \frac{1}{12}\Delta^2$. The complete equation for the Gaussian filter can be seen in Equation 2.6.[4] Note that other filters such as top-hat, spectral, Cauchy, and Pao can also be used in LES, but the Gaussian is given as:

$$G_{\Delta}^{\mathrm{Gaus}}(\boldsymbol{x}) = \left(\frac{6}{\pi\Delta^2}\right)^{3/2} \exp(-6x^2/\Delta^2). \tag{2.6}$$

The second LES step is to derive the equations for the evolution of the filtered velocity from the Navier-Stokes equations. These equations are presented in Equation 2.7:

$$\partial_t \tilde{\boldsymbol{u}} + \tilde{\boldsymbol{u}} \cdot \nabla \tilde{\boldsymbol{u}} = -\frac{1}{\rho}\nabla \tilde{p} + \nu \nabla^2 \tilde{\boldsymbol{u}} - \nabla \cdot \tau^{\Delta} \tag{2.7a}$$

$$\nabla \cdot \tilde{\boldsymbol{u}} = 0. \tag{2.7b}$$

Notice that all terms in this term are resolved, except for the term $\boldsymbol{\tau^{\Delta}}$ which is the SGS stress and is defined as $\tau^{\Delta} = \widetilde{u_i u_j} - \tilde{u}_i \tilde{u}_j$. That is, except for this term, all the other terms are functions of the filtered velocity which has been computed through application of the Gaussian filter. The remaining $\boldsymbol{\tau^{\Delta}}$ term is a residual quantity which must be accounted for in order for there to be closure of the filtered Navier-Stokes Equations.[4] Note that in the application of LES, this filtering operation would not be performed. Instead, motions above the coarse grid resolution scale, Δ, would be solved numerically just as in DNS. This filtering operation is only necessary when data exists below the coarse grid scale as would be the case for testing and evaluating LES models.

The third step is the modeling of the residual $\boldsymbol{\tau^{\Delta}}$ term, also known as the residual-stress tensor. This step is the crux of LES. There are a variety of commonly used models used to

estimate this SGS term. The modeled SGS stress term is henceforth referred to as $\tau^{\Delta,\mathrm{mod}}$ where mod refers to the specific model being used. The equation used to estimate this term can be seen in Equation 2.8:

$$\tau^{\Delta,\mathrm{mod}} \approx \tau^{\Delta} = \widetilde{u_i u_j} - \tilde{u}_i \tilde{u}_j \ . \qquad (2.8)$$

Notice that the SGS stress, $\boldsymbol{\tau}^{\boldsymbol{\Delta}}$, is thus defined as the difference between the filtered stress tensor field, $\widetilde{u_i u_j}$, and the stress tensor field of the filtered velocities, $\tilde{u}_i \tilde{u}_j$. The SGS models investigated in the present study include the Smagorinsky Model, Similarity Model, Mixed Model, Dynamic Model, Coherent Structures Model, and the Stretched Vortex Model.[13,14,15,16,17,18] These models are described in greater detail in the following sections.

In the fourth step, after the SGS stresses have been modeled, the filtered equations presented in Equation 2.7 are then solved numerically for the filtered velocity which then provides an approximation for the large-scale motions in one realization of the flow.[4]

*2.3.1 Subgrid-Scale Models*

The following section provides brief descriptions, background, and historical performance of the various SGS models used to estimate the SGS stress, $\boldsymbol{\tau}^{\boldsymbol{\Delta}}$, the different estimates are referred to by the notation $\boldsymbol{\tau}^{\boldsymbol{\Delta,\mathrm{mod}}}$, where mod refers to the name or abbreviation of the specific model. Evaluation of LES models is typically done either *a priori* or *a posteriori*. An *a priori* evaluation of a model is typically done by using fully resolved data (either experimental of DNS) to directly measure the modeling assumption, i.e. comparing the DNS or experimental $\boldsymbol{\tau}^{\Delta}$ with $\boldsymbol{\tau}^{\Delta,\mathrm{mod}}$. In an *a posteriori* evaluation, the SGS model is used to perform a calculation for the flow and the statistics of this flow are compared to DNS or experimental flow statistics.[4] The present study focuses primarily on *a priori* testing.

*2.3.2 Smagorinsky Model*

Perhaps the best known and most popular model for this residual stress tensor is known as the Smagorinsky model.[13,16] The Smagorinsky model is a turbulent viscosity model that models the anisotropic portion of the SGS stress tensor. The anisotropic, or deviatoric, portion of the stress can be seen in Equation 2.9:

$$\tau_{ij}^{\Delta,\mathrm{d}} = \tau_{ij}^{\Delta} - \frac{1}{3}\tau_{ij}^{\Delta}\delta_{ij}. \tag{2.9}$$

This deviatoric portion of the stress represents removing the trace from the SGS stress tensor. The model then proposes that the deviatoric portion of the SGS stress is approximately equal to the SGS stress, i.e., $\tau^{\Delta,\mathrm{smag}} \approx \tau^{\Delta,\mathrm{d}}$, as the isotropic portion is assumed to be negligible.[13] The actual model for the SGS stress is given in Equation 2.10:

$$\tau^{\Delta,\mathrm{smag}} = -2\nu_T\tilde{S}_{ij}. \tag{2.10}$$

Note the similarity between this model and the closure to the Reynolds stress in Equation 2.6 with the exception that instead of the mean rate of strain tensor, $\tilde{S}_{ij}$, refers to the filtered, or resolved rate of strain tensor. In other words, this rate of strain tensor is calculated using the velocity at scales larger than Δ. The equation for this tensor can be seen in Equation 2.11:

$$\tilde{S}_{ij} = \frac{1}{2}\left(\frac{\partial\tilde{u}_j}{\partial x_i} + \frac{\partial\tilde{u}_i}{\partial x_j}\right). \tag{2.11}$$

Just as with RANS, however, $\nu_T$ remains undetermined. To estimate this term, the Smagorinsky model uses the product of the Smagorinsky lengthscale, $l_s$, and the magnitude of the velocity difference at that lengthscale, $|\tilde{S}|$. The magnitude of this velocity difference is defined with respect to the filtered rate of strain tensor as $|\tilde{S}| \equiv \sqrt{\tilde{S}_{ij}\tilde{S}_{ij}}$. The Smagorinsky lengthscale is determined by the product of the LES filter width, Δ, and the Smagorinsky

coefficient, $C_s$.[3,7] This results in an expression for the turbulent viscosity as seen in Equation 2.12:

$$\nu_T = (C_s\Delta)^2\widetilde{S}. \qquad (2.12)$$

In principle, the Smagorinsky coefficient will depend on scale and is proportional to the filter width.[4] This model has proven to be computationally inexpensive, stable, and relatively simple. These attributes have led to its widespread use.[7]

In *a priori* testing, the model typically results in a correlation coefficient, $\rho$, between the fully resolved stress and the modeled SGS stress of between 0 and 0.25. This correlation goes up to around 0.4 when the modeled and fully resolved (via experimental or DNS data) SGS force, $\nabla \cdot \boldsymbol{\tau}^{\Delta}$, are compared. The correlation continues to rise to a typical value between 0.5 and 0.7 when the SGS dissipation rate, $\tau_{ij}^{\Delta}\tilde{S}_{ij}$ is considered.[7] The relative inconsistency in correlation coefficients however, indicate that this model does a poor job of accurately capturing the physics of the SGS flow. For this reason, the Smagorinsky is typically used as a means of comparing other SGS models. In a way, it is the base model used for comparison of how well another models works in capturing the physics of the flow.

### *2.3.3 Similarity Model*

The Similarity Model, proposed by Bandina *et al*. (1980), uses the concept of scale similarity to estimate the SGS stress.[14] In other words, the Similarity model operates on the assumption that the structure of the velocity field below the Δ scale is similar to the structure of the velocity field above the Δ scale.[7] This LES model reflects this by adding an additional filter to the resolved, coarse grid scale.[7] This additional filter, known as the similarity filter is denoted by an overbar, $\overline{(\ )}$. This filter is assumed to be directly related to the SGS stress behavior. The

length scale of the filter, $\Delta^{\text{sim}}$ is defined by $\Delta^{\text{sim}} = \gamma\Delta$ where $\Delta$ is the standard LES lengthscale and $\gamma$ varies between 1 and 2 depending on the specific study. The similarity filter can take a variety of shapes, but for the present study, this filter is a Gaussian convolution, just as with the first LES filter. The Similarity Model then estimates the SGS stress through Equation 2.13:

$$\tau_{ij}^{\Delta,\text{sim}} = C_{\text{sim}}\left(\widetilde{\overline{u}_i}\widetilde{\overline{u}_j} - \widetilde{\overline{u}_i}\widetilde{\overline{u}_j}\right). \tag{2.13}$$

Note that in this model, the trace of the SGS stress is not subtracted meaning that the isotropic portion of the SGS stress is not considered negligible.

In *a priori* testing of this model, SGS stress correlation with fully resolved data was as high as 0.8.[14] While at least some portion of this high correlation is likely due to filters' spectral overlap meaning that some data would be common between the modeled and fully resolved stresses. Liu *et al*. however concluded that this overlap contributed to only a small portion, about 0.2, of the overall correlation.[3,19] With this said, it is important to note that a significant downside to this model is that, as Bandina *et al.* showed, the model under predicted levels of SGS dissipation which could lead to would lead to incorrect simulation of the physics of the SGS flow.[7]

### *2.3.4 Mixed Models*

To offset the incorrect prediction of SGS dissipation in the Similarity model, Bandina *et al.* proposed a Mixed Model that included the simple superposition of the Similarity model with the existing Smagorinsky model, or simply $\tau_{ij}^{\Delta,\text{mix}} = \tau_{ij}^{\Delta,\text{sim}} + \tau_{ij}^{\Delta,\text{smag}}$.[14] The full equation for this mixed model is then given by Equation 2.14:

$$\tau_{ij}^{\Delta,\text{mix}} = C_{\text{sim}}\left(\widetilde{\overline{u}_i}\widetilde{\overline{u}_j} - \widetilde{\overline{u}_i}\widetilde{\overline{u}_j}\right) - 2(C_s\Delta)^2\tilde{S}\tilde{S}_{ij}. \tag{2.14}$$

Testing of this model showed that it behaved as intended in that the addition of the Smagorinsky model resulted in a more accurate prediction of the SGS dissipation while having a minimal impact on the SGS stress as the Similarity model's contribution to the SGS stress is typically much greater than the Smagorinsky model's.[7] Since this model reconciles shortcomings in both the Smagorinsky and the Similarity, it should perform better than each of its constituent models. With this said, it is important to note that turbulence modeling is complex and the accuracy of a model is often highly dependent on the LES length scale and the flow being observed.

*2.3.5 Dynamic Models*

One major shortcoming of the Smagorinsky, Similarity, and hence the Mixed Models is that the appropriate values for the coefficients $C_s$ and $C_{\text{sim}}$, changes with the flow regime being studied and also the specific type of flow.[4] For example, the appropriate Smagorinsky coefficient for laminar flow is 0 whereas the appropriate coefficient for high Reynolds number flows is nearly 0.15. To address this issue, Germano *et al.* proposed a model that provided a methodology for determining an appropriate local Smagorinsky coefficient.[4,15] To do this, the dynamic model uses the concept of scale invariance by applying the measured coefficient at resolved scales to the SGS range.[7] This procedure is based on the Germano identity given in Equation 2.15:

$$L_{ij}(\boldsymbol{x},t) = \tau_{ij}^{\alpha\Delta}(\boldsymbol{x},t) - \overline{\tau_{ij}^{\Delta}(\boldsymbol{x},t)}. \tag{2.15}$$

Note that in this identity, $L_{ij} = \overline{\widetilde{u_i}\widetilde{u_j}} - \overline{\widetilde{u}_i}\overline{\widetilde{u}_j}$, and the overbar indicates test filtering at the scale $\alpha\Delta$.[7] The $\tau_{ij}^{\alpha\Delta}$ and $\tau_{ij}^{\Delta}$ terms in this equation can then be replaced with the appropriate Smagorinsky models to yield the expression below:

$$L_{ij} - \frac{1}{3}L_{kk}\delta_{ij} = (C_s^{\Delta})^2 M_{ij}, \quad \text{where} \tag{2.16a}$$

$$M_{ij} = -2\Delta^2 \left[\alpha^2 \left(\frac{C_s^{\alpha\Delta}}{C_s^{\Delta}}\right)^2 |\bar{\tilde{S}}|\bar{\tilde{S}}_{ij} - \overline{|\tilde{S}|\tilde{S}_{ij}}\right]. \quad (2.16b)^7$$

The most common choice for α is 2 and it is explicitly assumed that there is scale invariance at this level such that $C_s^{2\Delta} = C_s^{\Delta}$. This assumption allows for $M_{ij}$ to be fully resolved at the LES scale. Furthermore, since Equation 2.16a must hold true for the five independent tensor elements (note the trace has been subtracted), the system is overdetermined. This means that one $C_s^{\Delta}$ cannot satisfy the equation exactly. This means that the equation can only hold true in the average sense.[7] Different versions of the dynamic model enforce this condition differently. The most widely used approach to enforcing the condition was proposed by Lilly (1992) is based on minimizing the square error $E = \langle\left[L_{ij} - (C_s^{\Delta})^2 M_{ij}\right]^2\rangle$.[16] This method leads to calculating the Smagorinsky coefficient via Equation 2.17:

$$(C_s^{\Delta})^2 = \frac{\langle L_{ij}M_{ij}\rangle}{\langle M_{ij}M_{ij}\rangle}. \quad (2.17)$$

Note that in this equation, $\langle\ \rangle$, indicates an ensemble average. Without this averaging, it has been shown that the model yields a highly variable turbulent viscosity field.[20] The coefficients computed in Equation 2.17 are used directly in Smagorinsky model in Equation 2.10 and result in the estimation of the SGS stress by Equation 2.18:

$$\tau^{\Delta,\text{smag,dyn}} = -2\frac{\langle L_{ij}M_{ij}\rangle}{\langle M_{ij}M_{ij}\rangle}\Delta^2\widetilde{S}. \quad (2.18)$$

Note that while this model provides a more accurate estimation of the SGS stress than the Smagorinsky model as it dynamically adjusts the coefficients appropriately, it is also significantly more computationally expensive as it must determine the local Smagorinsky coefficient as opposed to specifying one coefficient for the flow being studied. Additionally, in flows with complex geometry, the statistical homogeneity necessary for the averaging process in Equation 2.17 is a poor assumption. This has given rise to other forms of the Dynamic Model.[7]

*2.3.6 Dynamic Mixed Models*

One variation of the Dynamic model attempts to combine apply the dynamic modeling of coefficients to the similarity model coefficient in addition to the Smagorinsky coefficient creating a Dynamic Mixed Model. In this model, proposed by Vreman *et al.*, the coefficients are determined by minimizing the error in the Germano identity (Equation 2.15) which leads to a 2 x 2 system of equations that can be solved for $C_s$ and $C_{sim}$.[7] In *a priori* testing of this model, it was found to be superior to both the Dynamic and the Mixed Model, but the addition of the second dynamic coefficient tends to diminish the SGS stress correlations.[7] For this reason, the Dynamic Mixed Model is not considered in the present study.

*2.3.7 Coherent Structures Model*

An interesting and promising model developed by the Center for Turbulence Research is the Coherent Structures Model, CSM. Like the Smagorinsky model, the CSM is an Eddy Viscosity Model following the same form as Equation 2.10. As such, the CSM is defined by Equation 2.19:

$$\tau^{\Delta,\mathrm{CSM}} = -2\nu_T \tilde{S}_{ij}. \tag{2.19}$$

In this model, the eddy, or turbulent, viscosity is defined as

$$\nu_T = C_{CS}\Delta^2\tilde{S}. \tag{2.20}$$

The model, introduced by Kobayashi, provides a method for relating regions of higher vorticity to regions of higher eddy viscosity.[17] To do this, the model uses $Q$, the full second invariant of a full flow field. For the full DNS or experimental flow field, this second invariant is given by Equation 2.21:

$$Q_{\mathrm{DNS}} = \frac{1}{2}\left(W_{ij}W_{ij} - S_{ij}S_{ij}\right) = -\frac{1}{2}\left(\frac{\partial u_j}{\partial x_i}\frac{\partial u_i}{\partial x_j}\right). \tag{2.21}[17]$$

In this equation, $W_{ij}$ is the vorticity tensor and is defined in Equation 2.22:

$$W_{ij} = \frac{1}{2}\left(\frac{\partial u_j}{\partial x_i} - \frac{\partial u_i}{\partial x_j}\right). \quad (2.22)$$

For the CSM, the individual terms in this second invariant of the velocity field are filtered at the LES scale to give Equation 2.23:

$$Q = \frac{1}{2}\left(\widetilde{W}_{ij}\widetilde{W}_{ij} - \tilde{S}_{ij}\tilde{S}_{ij}\right) = -\frac{1}{2}\left(\frac{\partial \tilde{u}_j}{\partial x_i}\frac{\partial \tilde{u}_i}{\partial x_j}\right) \quad (2.23)$$

The sign of this second invariant gives an indication of how the flow is behaving. For $Q > 0$, the vorticity term dominates indicating that the region of flow has a stronger rotation than strain. For this reason a positive Q can be interpreted as a vortex tube.[7] When Q is negative, the flow is experiencing greater strain than vorticity or rotation. In the CSM, Kobayashi normalizes the second invariant with the filtered velocity gradient tensor, $\frac{\partial \tilde{u}_i}{\partial x_j}$, to obtain a Coherent Structures Function, $F_{CS}$. The resulting equations can be seen in Equations 2.24 and 2.25:

$$E = \frac{1}{2}\left(\widetilde{W}_{ij}\widetilde{W}_{ij} + \tilde{S}_{ij}\tilde{S}_{ij}\right) = -\frac{1}{2}\left(\frac{\partial \tilde{u}_j}{\partial x_i}\right)^2, \quad (2.24)$$

$$F_{CS} = \frac{Q}{E}. \quad (2.25)$$

This coherent structures function is then used in combination with an empirically optimized value $C_1 = \frac{1}{22}$ ,and the energy decay suppression function $F_\Omega = 1 - F_{CS}$ to determine the full CSM coefficient given in Equation 2.26:

$$C_{CS} = C_1|F_{CS}|^{3/2}F_\Omega. \quad (2.26)[17]$$

Kobayashi developed this model using turbulent channel flow, but *a-posteriori* testing has since been conducted on the model using a variety of complex non-homogeneous flows. The model has historically performed comparably to the Dynamic Smagorinsky Model in terms of estimating the SGS stress, but has exhibited better efficiency and numerical stability.[17]

*2.3.8 Stretched Vortex Model*

Another interesting and promising LES model is the Stretched Vortex Model, SVM, proposed by Misra and Pullin (1996).[18] This model is based on the idea of structure-based Reynolds stress closure, and asserts that the SGS structure of the turbulence is composed of stretched vortices whose orientations are determined by the resolved velocity field.[18] The model ultimately relates the SGS stress to the structure orientation of these vortices and the SGS kinetic energy, which together, with an assumed Kolmogorov energy spectrum of the SGS vortices, provides closure to the Navier-Stokes equations at the resolved scales. Furthermore, in the model, the flow within each computational cell is assumed to result from an ensemble of straight, nearly axisymmetric vortices that are aligned with the local resolved rate of strain tensor. The subgrid spiral vortices are thus local approximate solutions to the exact Navier-Stokes equations.[21] The SGS stress in this model is given by Equation 2.27:

$$\tau_{ij} = \bar{\rho}\tilde{k}\left(\delta_{ij} - e_i^v e_j^v\right). \qquad (2.27)$$

In this equation, $\tilde{k}$ represents the subgrid energy and is given by , $\tilde{k} = \int_0^\infty E(k)dk$ and $\boldsymbol{e}^v$is the unit vector aligned with the subgrid vortex axis. In this model, the subgrid vortex, i.e. $\boldsymbol{e}^v$ is presumed to be aligned with the principal extensional eigenvector of the resolved rate of strain tensor, $\tilde{S}_{ij}$, as given in Equation 2.11. The subgrid energy is estimated by assuming a spiral subgrid vortex whose Kolmogorov-like energy spectrum is given by Equation 2.28:

$$E(k) = K_0\epsilon^{2/3}k^{-5/3}\exp[-2k^2\nu/(3|\tilde{a}|)]. \qquad (2.28)^{21}$$

In this expression, $K_0$ is the Kolmogorov prefactor, $\epsilon$ is the local cell-averaged dissipation for the resolved and subgrid scale, $\nu$ is the kinematic viscosity, and $\tilde{a} = S_{ij}e_i^v e_j^v$ is the axial strain along the subgrid vortex axis.[21] The first two terms in Equation 2.28, $K_0\epsilon^{2/3}$, can be grouped together and calculated via Equation 2.29:

$$K_0\epsilon^{2/3} = \frac{\overline{F_2}(\Delta)}{\Delta^{2/3}A}\text{, where} \tag{2.29a}$$

$$\overline{F_2}(\Delta) = \frac{4}{\Delta}\int_0^{\pi} E(s/\Delta)\left(1 - \frac{\sin s}{s}\right)ds\text{ , and} \tag{2.29b}$$

$$A = 4\int_0^{\pi} s^{-5/3}(1 - s^{-1}\sin s)ds \approx 1.90695. \tag{2.29c}$$

In this set of equations, $\overline{F_2}(\Delta)$ is a second order velocity structure function averaged over the surface of a sphere with radius $\Delta$ corresponding to the LES grid spacing. In the present study, this term is estimated using a six point stencil of the resolved velocity components as shown in Equation 2.30:

$$\overline{F_2}(\Delta) = \frac{1}{6}\sum_{l=1}^{3}\sum_{m=1}^{3}(\delta^2\tilde{u}_l)_m\text{ , where} \tag{2.30a}$$

$$(\delta^2\tilde{u}_l)_m = \left(\tilde{u}_l(\boldsymbol{x} + e_m\Delta x_m) - \tilde{u}_l(\boldsymbol{x})\right)^2 + \left(\tilde{u}_l(\boldsymbol{x} + e_m\Delta x_m) + \tilde{u}_l(\boldsymbol{x})\right)^2. \tag{2.30b}$$

Note that in this equation, $e_m$ does not refer to the subgrid vortex alignment direction but is instead simply the Cartesian direction.[21]

Testing of this model has yielded reasonable results (see Pantano 2008 and Misra 1997) indicating that the physics in the SGS range are at least somewhat captured by these subgrid vortex structures. With this said, the eddy-viscosity models do hold a significant advantage over this spectral model in that they are much simpler to implement.[18,21]

# Chapter 3

# EXPERIMENTAL SETUP AND METHODOLOGY

Historical approaches to experimental LES SGS model evaluations, as well as the design and hardware of the Three-Dimensional Particle Tracking Velocimetry (3DPTV) system and flow facility used in the present study are described in this chapter. This includes a brief description of 2-dimensional particle displacement velocimetry (PDV), 3-dimensional holographic particle image velocimetry (HPIV), the modification of a defocusing digital particle image velocimetry (DDPIV) method, and the design of the 3DPTV system. It also includes a description of the water tunnel used, the optical and camera system, illuminations sources, and calibration equipment. The process through which data were collected is also discussed. Note that much of the following information is included in Dona's "Implementation of 3DPTV for turbulence analysis and subgrid-scale stress model testing of a backward-facing step flow" and Grothe's "Modification of a DDPIV System for Imaging Small Volumes Using Triangulation for Particle Identification."[3,22]

## 3.1 Historical Experimental Approaches

Historically, much LES SGS model evaluation was conducted using high resolution DNS 3-Dimension 3-Component (3D3C) velocity vector fields. The DNS vector fields are excellent sources for providing high resolution data to calculate the SGS stress directly and compare with LES model for low Reynolds number and simple geometric flows.[7] For reasons addressed in

Section 2.1, DNS becomes much more computationally expensive as Reynolds number increases. For this reason, experimental approaches are more practical for evaluating LES models for high Reynolds number and complex flows. With this said, experimental approaches often sacrifice spatial resolution for the ability to analyze high Reynolds number flows. A variety of experimental approaches for a range of flows and Reynolds numbers have been conducted by Charles Meneveau and Joseph Katz of Johns Hopkins University, henceforth referred to as KM. These studies were focused on studying flow as high of a Taylor-microscale Reynolds number, $Re_\lambda$, (sometimes referred to as the turbulent Reynolds number) as defined in Equation 3.1:

$$Re_\lambda \equiv \frac{u\prime\lambda}{\nu}\text{, where} \tag{3.1a}$$

$$\lambda \approx u'\sqrt{\frac{15\nu}{\varepsilon}} \approx \sqrt{\frac{15\nu l}{u\prime}}. \tag{3.1b}$$

In this set of equations λ is known as the Taylor Microscale, *u'* refers to the estimated velocity fluctuations, *l* is a characteristic length scale, ν is the kinematic viscosity, and ε is dissipation.[4] The following section focuses on the findings of Katz and Meneveau's studies and how they shaped the present system.

### *3.1.1 Two-Dimensional PDV*

A major objective of Katz and Meneveau's studies was to generate turbulent flow with a high $Re_\lambda$ within a moderately sized facility.[20] KM achieved this by looking at the far field flow of a turbulent jet. Specifically, KM looked at a 6.3 mm diameter round jet 193 diameters downstream. In doing so, this resulted in a high length scale, *l*, of approximately 7 cm which, as per Equation 3.1, helped increase the Taylor Microscale and thus the turbulent Reynolds number. Furthermore, the fluctuating component of velocity at this location was determined to be 0.09 m/s, or 18% of the mean velocity as per Pope 2000. These parameters resulted in a turbulent

Reynolds number, $Re_\lambda \approx 310$, thereby achieving their goal of generating a high turbulent Reynolds number within a moderate-sized facility.[20]

To experimentally obtain the velocity field from this flow, KM used a technique known as particle displacement velocimetry (PDV), or what has become known as Particle Image Velocimetry (PIV). This technique involves a laser light source illuminating particles at two separate instances of the flow. In the case of KM (1993), these two instances were imaged onto film and converted to a 5000 x 5000 pixel array and velocity vectors for 64 x 64 pixel arrays are generated using an autocorrelation method. This corresponded to a 1.1 x 1.1mm window in that actual flow field.[20]

As previously mentioned, one of the key challenges for KM's experimental approach was to achieve a sufficiently high resolution of the velocity field that could then be used to properly pursue turbulence modeling. The smallest length scale of the flow is determined by the Kolmogorov length scale, $\eta$, which corresponds to the length scale of the smallest eddies in the flow. The size of this length scale is related to the turbulent Reynolds number and can be approximated through Equation 3.2:

$$\eta \approx \left(\frac{\nu^3 l}{u'^3}\right)^{1/4}. \qquad (3.2)^4$$

Given the Kolmogorov length scale, Pope (2000) also cites that for evaluating SGS stress models, the flow field resolution should correspond to a grid spacing, $\delta$, of approximately $2.1\eta$.[4]

In KM's initial 2-dimensional PDV vector fields, the vector grid spacing was 1.1mm and the Kolmogorov length scale for the flow analyzed was 0.1mm. This corresponded to $\delta = 10\eta$. This meant that the dissipation range of the smallest eddies were not resolved. In this study, KM conduct an *a priori* test of the Smagorinsky model, but it is important to note that the $\delta = 2.1\eta$ criterion was not satisfied.[20] This, combined with the only capturing 2-dimensions of the 3-

dimensional flow were the major shortcomings of this study and provided grounds for additional research in a 3-dimensional, higher resolution system.

### *3.1.2 Three-Dimensional Holographic PIV*

In 2000, to alleviate some of the shortcomings of the 2-dimensional PDV method, Katz and Meneveau used holographic particle image velocimetry (HPIV). This method is a PIV method, similar to the PDV used in the previous study, that utilizes two perpendicular, double exposure holograms recorded simultaneously. From the double exposure of the holograms, a three-dimensional velocity vector field can be developed by an autocorrelation of the two exposures.[23]

In this HPIV study, the turbulent flow studied was the core region of a square duct at a Reynolds number of $1.2 \times 10^5$. The flow had a Taylor micro-scale Reynolds number of approximately 260, which is smaller than the turbulent Reynolds number for the far field of the turbulent jet as the length scale for the duct was smaller than the length scale in the far field of the jet. The Kolmogorov length scale for the duct flow was determined to be approximately 0.1mm, just as with the turbulent jet. With the HPIV system, however, KM were able to achieve a velocity vector field with a resolved grid spacing of 0.33 mm.[23] This meant that $\delta \approx 3.3\eta$ which is much closer to the criterion prescribed in Pope (2000) of $\delta = 2.1\eta$. With this resolution KM were able to better capture the smaller eddies in the flow. This lends more validity to the *a priori* testing in the study, but still leaves room for resolution improvement.

*3.1.3 Argument for a 3DPTV Method*

While the HPIV method used in KM is capable of producing extremely accurate velocity fields and is capable of providing sufficient resolution, the physical setup of the system is extraordinarily difficult and sensitive. The system is very sensitive to slight environmental disturbances and is incredibly time consuming to produce a single velocity field.[22] In addition, non-holographic, camera-based 3D velocimetry methods are becoming more prevalent, and therefore it is of interest to develop a 3DPTV system, based on this approach, for pursuing experimental turbulence modeling. For this reason, the present study pursues the development of a 3DPTV method that would allow these types of studies. In this approach, the 3DPTV method will be able to track particles in a Lagrangian sense using an epipolar line search triangulation methodology. Though the method requires precise alignment, calibration methods can accommodate for deviations from true alignment. Furthermore, when cameras with adequately high resolution are used, the method is capable of resolving near the Kolmogorov length scales for moderately high Taylor micro-scale Reynolds numbers. This method is described in further detail in the following section.

**3.2 The Design of a 3DPTV System for Evaluating LES Models**

In his 2008 Master's thesis at the University of Washington, Rob Grothe developed the theoretical constructs of the 3DPTV system by developing a full 3D characterization of the defocusing digital particle image velocimetry (DDPIV) method, which is explained below in the remainder of this section.[22] The DDPIV method relies on how focused a particle appears on the image plane through three different apertures to determine the three-dimensional location. The initial implementation of the DDPIV triply exposed a single CCD, which limited the number of

particles that could be imaged and accurately identified. Subsequent implementations used three individual charge-coupled devices (CCDs) instead of three apertures to determine the three dimensional location of particles.[24,25,26,27] While successful, in an effort to obtain higher resolutions, the Dabiri group developed a particle tracking version of DDPIV. A schematic of this 3DPTV approach can be seen in Figure 3.1.

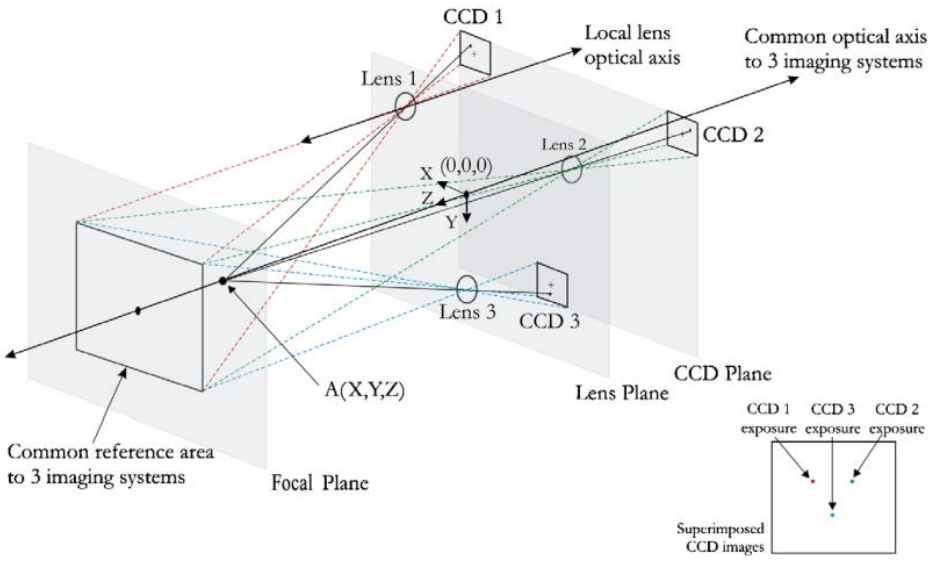


Figure 3.1: 3DPTV System Schematic[22]

When implemented, this three-camera system allowed for the imaging of a skewed rectangular prism, known as the volume of interest (VOI). How ray-tracing creates this VOI and its shape can be visualized in Figures 3.2 and 3.3.

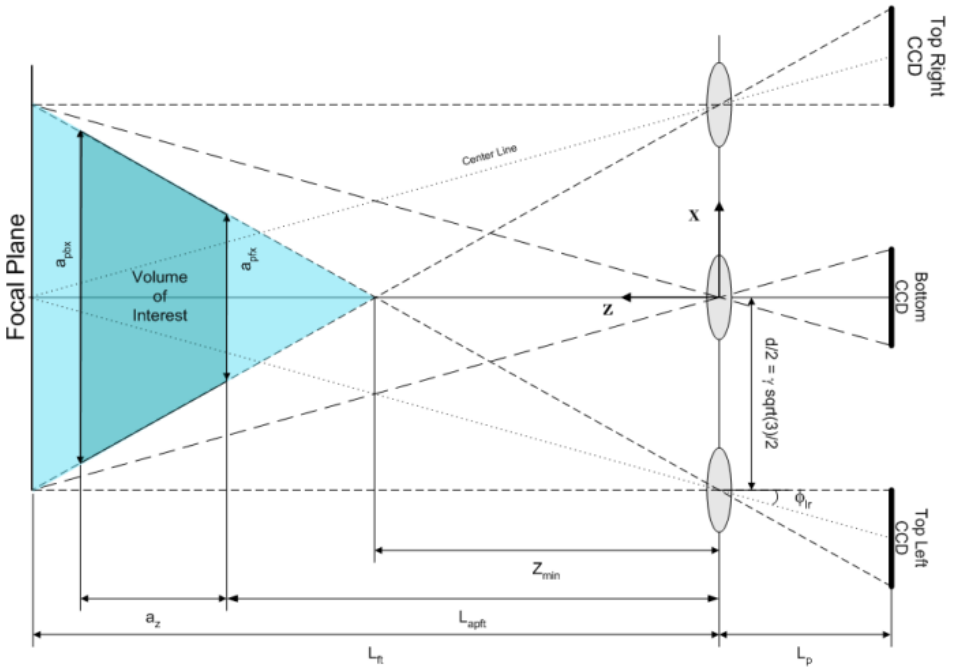


Figure 3.2: 3DPTV imaged volume defined in the *X*-*Z* plane[22]

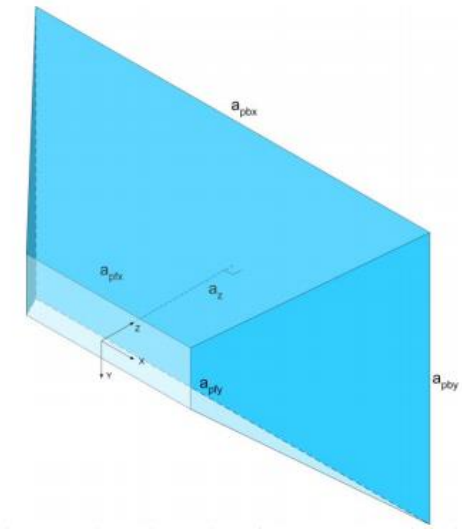


Figure 3.3: Three-dimensional view of imaging volume[22]

If the system were to be implemented in only one medium, such as only air or only water, determination of the focal plane would come from application of the simple thin-lens equation

$\frac{1}{f} = \frac{1}{L_{ft}} + \frac{1}{L_p}$, where $f$ is the focal length of the lens, $L_{ft}$ is the distance from the lens to the focal plane along the optical axis, and $L_p$ is the distance from the lenses to the CCD sensors along the optical axis. However, the system was not designed to be used in only one medium, and was modified with a water-filled prism to adjust for the refraction inherent in imaging in water, acrylic, and air. A schematic of the system's relevant parameters for one CCD can be seen in Figure 3.4.

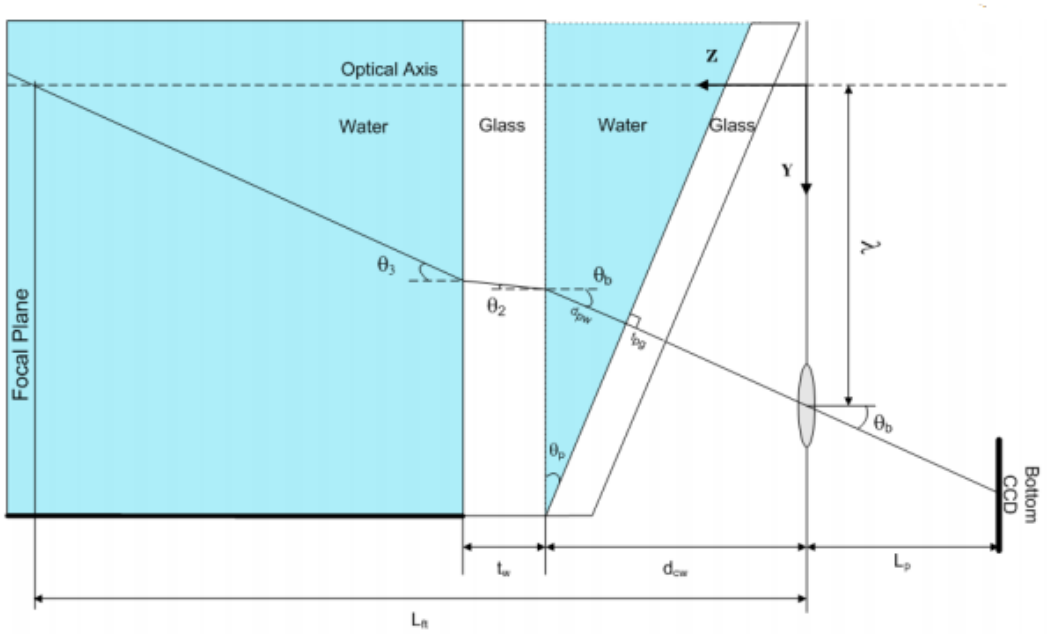


Figure 3.4: 3DPTV Design Parameters[4]

The addition of the parameters associated with refraction complicates determination of the system's focal plane and CCD placement. For determining the focal distance, the Ray Transfer Matrix (RTM) presented in Equation 3.3 must be used.

$$\begin{pmatrix} x_f \\ \theta_f \end{pmatrix} = M \begin{pmatrix} x_i \\ \theta_i \end{pmatrix} = \begin{pmatrix} A & B \\ C & D \end{pmatrix} \begin{pmatrix} x_i \\ \theta_i \end{pmatrix}. \tag{3.3}$$

In this equation, $x$ is the off-axis distance from a ray to the lens optical axis and $\theta$ is the off-axis angle from the lens optical axis. The values of *A, B, C,* and *D* provide information on the medium through which the ray is travelling. In Grothe (2008), the full matrix, *M*, is determined for the 3DPTV system for a ray starting at the CCD plane, travelling to and through the lens, through the air, experiencing refraction at the air-glass interface, and at the glass-water interface. This expression is presented in Equation 3.4.

$$M = \begin{pmatrix} 1 & L_{ft} - d_{cw} - t_w \\ 0 & 1 \end{pmatrix} \begin{pmatrix} 1 & 0 \\ 0 & \frac{\eta_g}{\eta_w} \end{pmatrix} \begin{pmatrix} 1 & t_w \\ 0 & 1 \end{pmatrix} \begin{pmatrix} 1 & 0 \\ 0 & \frac{\eta_{pw}}{\eta_g} \end{pmatrix} \begin{pmatrix} 1 & d_{pw} \\ 0 & 1 \end{pmatrix} \begin{pmatrix} 1 & 0 \\ 0 & \frac{\eta_{pg}}{\eta_w} \end{pmatrix} \begin{pmatrix} 1 & t_{pg} \\ 0 & 1 \end{pmatrix} \begin{pmatrix} 1 & 0 \\ 0 & \frac{\eta_a}{\eta_{pg}} \end{pmatrix} \begin{pmatrix} 1 & d_{cw} - d_{pw} - t_{pg} \\ 0 & 1 \end{pmatrix} \begin{pmatrix} 1 & 0 \\ -\frac{1}{f} & 1 \end{pmatrix} \begin{pmatrix} 1 & L_p \\ 0 & 1 \end{pmatrix}. \quad (3.4)$$

This equation, $L_{ft}$, $d_{cw}$, $t_w$, $L_p$, and $t_{pg}$ are all defined in Figure 3.2 and $\eta_g$, $\eta_a$, $\eta_w$, and $\eta_{pg}$, are the indices of refraction for glass, air, water, and the prism glass respectively. The distance from the lens to the focal plane, $L_{ft}$, can then be determined by using Equation 3.4 in Equation 3.3 and solving for $L_{ft}$. This results in Equation 3.5:

$$L_{ft} = (d_{cw})\left(1 - \frac{\eta_w}{\eta_a}\right) + t_w\left(1 - \frac{\eta_w}{\eta_a}\right) + \left(\frac{f \cdot L_p}{L_p - f}\right)\left(\frac{\eta_w}{\eta_a}\right). \quad (3.5)$$

After this focal length is determined, the angle a light ray travels toward the CCD such that the intersection of the ray, the optical axis, and the focal plane is centered on the focal plane, as presented in Grothe (2008), can be determined through Equation 3.6:

$$\lambda = d_{cw}\tan\theta_b + t_w\left(\frac{\eta_a}{\eta_g}\right)\frac{\sin\theta_b}{\sqrt{1-\frac{\eta_a}{\eta_g}\sin\theta_b}} - \left(d_{cw} - L_{ft} + t_w\right)\left(\frac{\eta_a}{\eta_w}\right)\frac{\sin\theta_b}{\sqrt{1-\frac{\eta_a}{\eta_w}\sin\theta_b}}. \quad (3.6)$$

This equation for λ, the Y-offset from the optical axis, can then be solved numerically for $\theta_b$, the angle the ray makes with the optical axis. These equations were solved iteratively and implemented using the hardware described in the following sections.

## 3.3 Flow Facility

### *3.3.1 Test Section and Flow Settings*

The flow facility used in this study was a 6” x 12” (15.24 cm x 30.48 cm) Shear Layer Water Tunnel built by Engineering Laboratory Design, Inc. The facility, in its present configuration, can be seen in Figure 3.5 below.

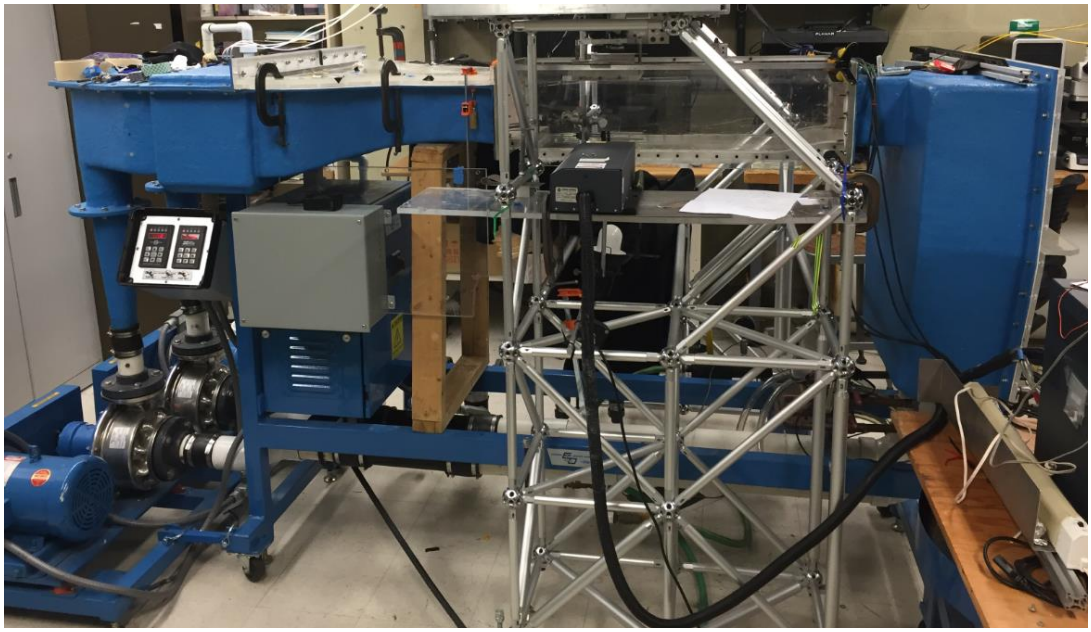

Figure 3.5: Engineering Laboratory Design, Inc. Shear Layer Water Tunnel

The tunnel is equipped with two 3 HP pumps capable of providing a maximum flow velocity of 3.28 fps (1.00 m/s). The maximum pump RPM for each motor is 1770 RPM, and the pump setting slope was calibrated for the range used in the present study.[3] Dye visualizations were performed at the test section’s center to determine the tunnel’s mean velocity, and the operating slope was determined to be 15.5 RPM/(cm/s).[3]

Additionally, the tunnel was fitted with a 36.00” (91.44 cm) removable test section. In the present experiment, the constant area rectangular test section was replaced with a backward-

facing step of height, h, of 2.8575 cm. This backward-facing step test section can be seen in Figure 3.6.

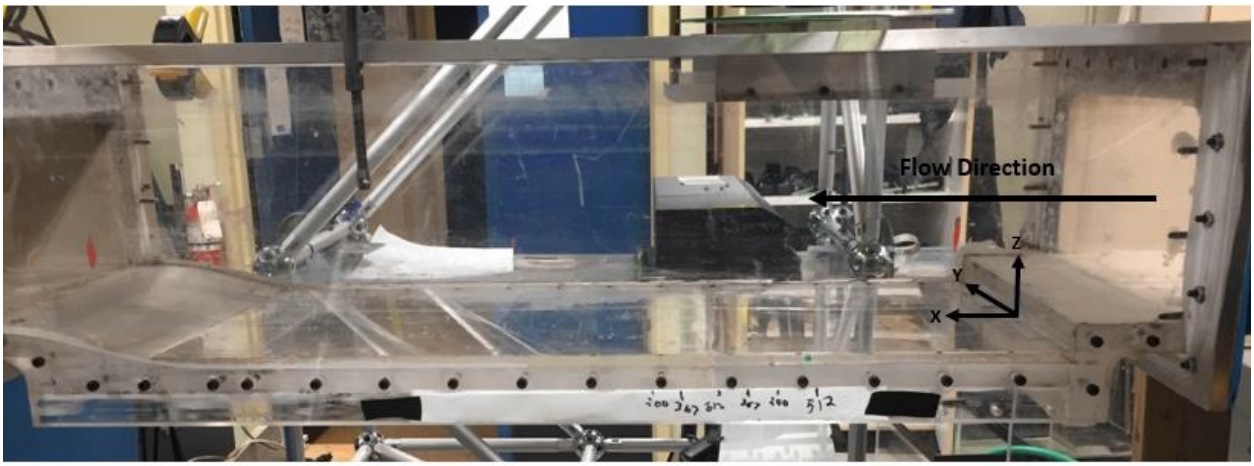


Figure 3.6: Water tunnel test section containing backward-facing step

The mean flow velocity used in the present study was 0.22 m/s (corresponding to a pump motor setting of 341 RPM). This resulted in a Reynolds number, $Re_h$=6274 as defined by Equation 3.7 below where $U_\infty$ is the freestream velocity, $h$ is the step height, and $\nu$ is the kinematic viscosity:

$$Re_h \equiv \frac{U_\infty h}{\nu}. \tag{3.7}$$

For a backward-facing step, and a Taylor microscale Reynolds number of $Re_\lambda$=130, as defined in Equation 3.1. This flow setting and Reynolds number was selected due to flow facility constraints, CCD resolution, and multi-phase flow limits. The flow facility was limited to a maximum flow velocity of 1 m/s placing an obvious limit on the freestream velocity. The multiphase flow limits were determined by the maximum number of particles that could be imaged on a 4008 x 2672 CCD where the overall system magnification of 1.2 led to an imaged particle diameter of 7 pixels. This will be described in further detail in the ensuing chapter. When combined with the guidance by Pope (2000) of a fluctuating velocity, *u'*, of 18% of the mean

flow velocity, the Kolmogorov length scale, corresponding to the length scale of the smallest eddies in the flow, was determined to be $\eta$=147 µm as estimated using Equation 3.2. In this case, $l$ is the characteristic length scale of the geometry associated with the flow, i.e. the height of the step, $h$.

### *3.3.2 Volume of Interest*

The Volume of Interest, VOI, for the present study was a skewed rectangular located 6.5h downstream of the backward-facing step with the bottom of the VOI being 13 mm above the bottom of the test section. The coordinate system and VOI can be seen in Figure 3.7.

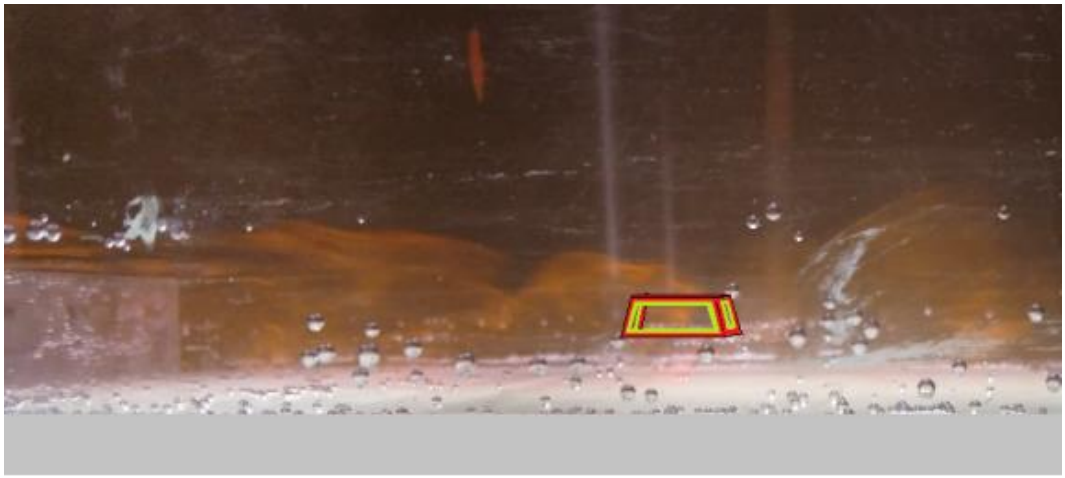

Figure 3.7: Approximate location of VOI (note flow is from left to right)[3]

Note that this VOI was centered in the Y-dimension. The VOI was 4.5mm deep in the Z direction. Note that, in this section, capital X,Y,Z are used to denote coordinates in real space, while lower case x, y are used to denote CCD pixel values. The bottom plane dimension was 30.49mm x 20.30mm, while the top plane dimension was 29.71mm x 19.81mm. The bottom plane was located 13 mm from the bottom of the step. The size and shape of the VOI was

determined by optical system constraints such that the camera system was capable of resolving motions close to the Kolmogorov length scale. Specifically, this size was set such that it would be comparable to that of Direct Numerical Simulation, DNS, approaches which, at the finest scales, have a spatial resolutions of $\delta = 2.1\eta$.[4] For further details on the shape of the VOI see Grothe (2008).

### *3.3.3 Particle Siphon System*

In addition to the installation of the backward-facing step geometry, a particle siphon system was designed and installed in the flow facility. Three 5mm diameter holes were drilled just upstream of the test section. Each of the holes were located at the same X location with the center hole being centered in the Y dimension with the other two holes being approximately 25 mm on either side. Hollow 4mm diameter metal wands were then inserted into each of these holes and connected via approximately 1 m of tubing. The metal wands were fixed in place after using dye visualizations to determine the optimal location to allow for even dispersion of particles. The tubing was then connected to three seeding bottles. The bottles were placed approximately 65cm above the seeding location to allow particles to flow freely with a gravity siphon after seeding bottles were squeezed. An image of this particle siphon system can be seen in Figure 3.8.

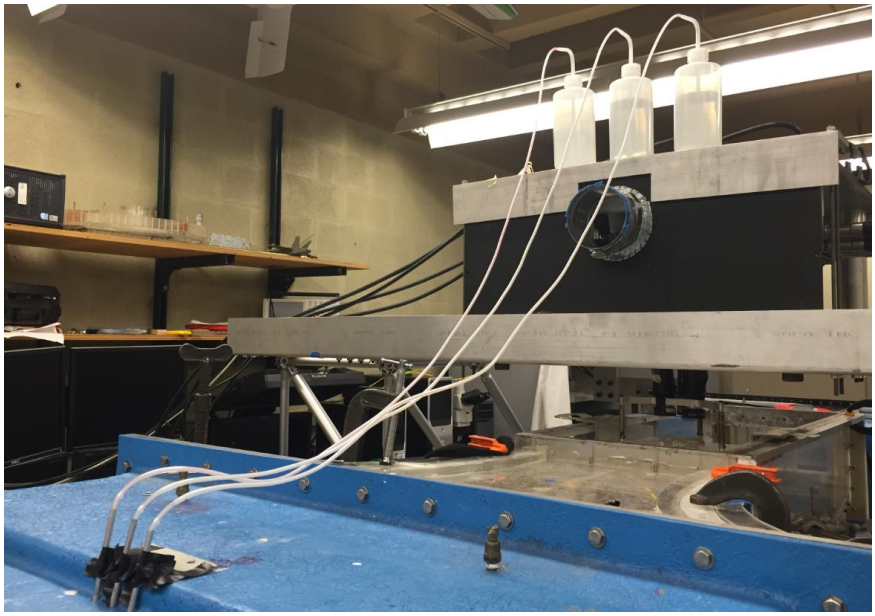

Figure 3.8: Particle Siphon/Seeding System

### 3.4 Optical/Camera System

The camera system used in this study consisted of three 4008x2672 CCD cameras. This was the same system used by Dona. Each of these three CCDs were mounted on 6-axis translation stages made by Thorlabs. The CCDs, along with the lens assemble, were mounted to form an equilateral triangle with the CCD triangle sides being 12 cm and the lens triangle sides being 6 cm. Black plastic and paper were both used to form a cone between the CCD and the lenses to shroud the CCD from seeing extra light. For information on the design and specification of the optical and camera system beyond what is presented in the following section, see Grothe (2008).[22]

### *3.4.1 Charge-Coupled Devices (CCDs)*

The cameras used in the present study were high-resolution area scan Illunis XMV-11000 grayscale cameras. Each of the cameras contained interline transfer CCDs with a resolution of 4008x2672. The CCDs have a well depth of 60,000 electrons, a signal-to-noise ratio of 30 dB and 9 micron square pixels. The CCDs are capable of capturing a Triggered Double Exposure (TDE). This meant that, despite the maximum frame rate of 3.8 Hz, the cameras are capable of taking consecutive exposures with as little as an 800 ns separation.[28] This is specifically tailored for PIV/PTV type applications as it allows an image pair to have a very small $\Delta t$ between sequential image pairs. The system would theoretically be capable of imaging flows with peak velocities around 90 m/s with a reasonable 10-pixel displacement.[3] Each of the three CCDs were mounted on 6-stage translation stages. The CCD and camera mounts can be seen in Figure 3.9.

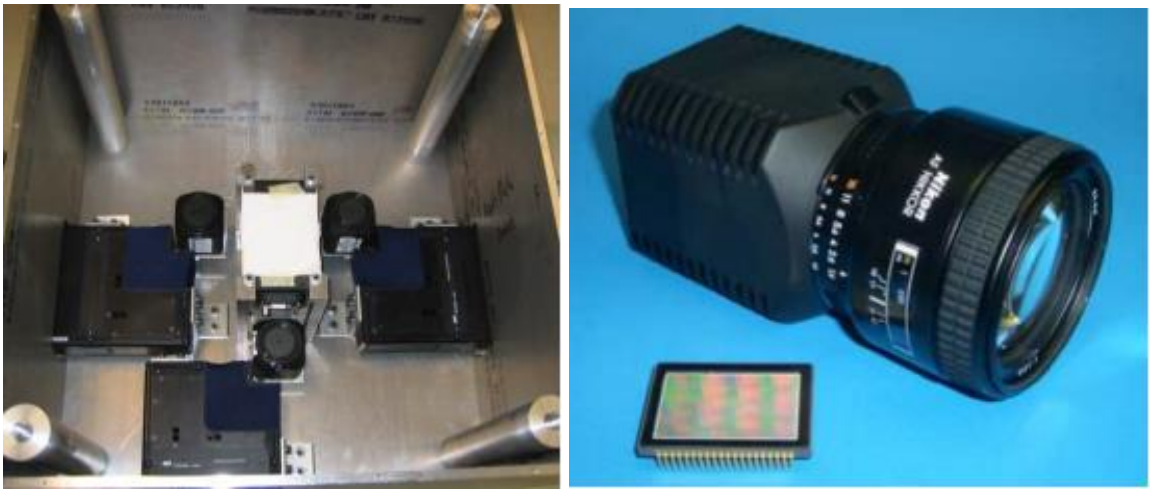

(a) CCDs mounted on 6-axis translation stage (b) Illunis XMV-11000 CCD

Figure 3.9: CCDs and mounts used in the present study[3]

*3.4.2 Lenses*

The lenses used in the system were Schneider-Kreunach Optics Macro-Symmar HM 120mm f/5.6 lenses. These lenses were chosen due to their precise focal length of 119.9mm +/- 1%, greater than 90% transmittance of the visible spectrum, and minimal edge distortion. Each of these properties resulted in a low level of error propagation to the rest of the system.[29] A cross section of this lens can be seen in Figure 3.10.

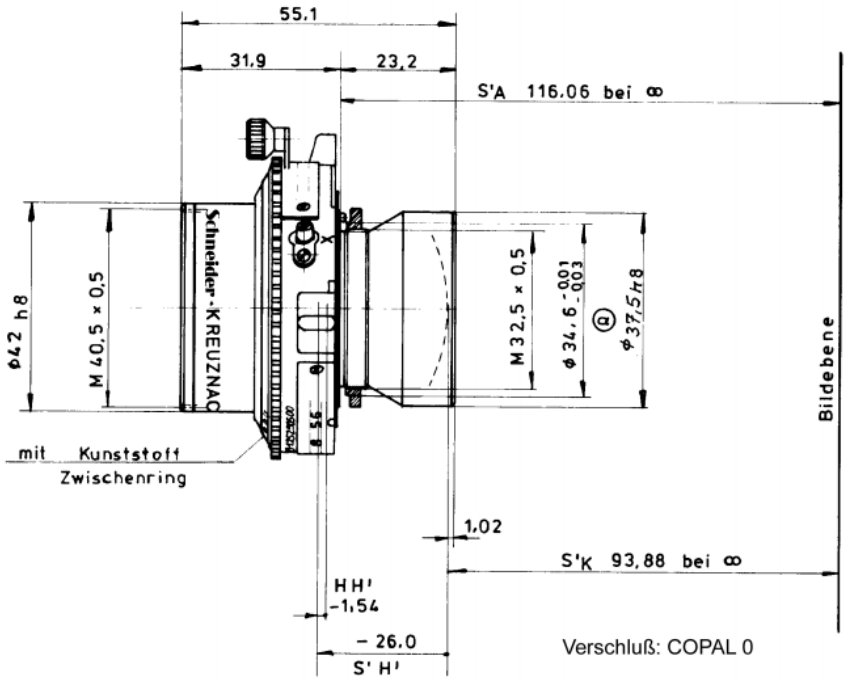


Figure 3.10: Schneider-Kreunach Optics Macro-Symmar HM Lens cross section[30]

*3.4.3 Water-Filled Prism*

To appropriately image the particles in the VOI, it is necessary to image through three media, the water in the tunnel, the acrylic top, and air. Since there is significant refraction through these three media, without correction, particle images would result be distorted as shown in Figure 3.11.

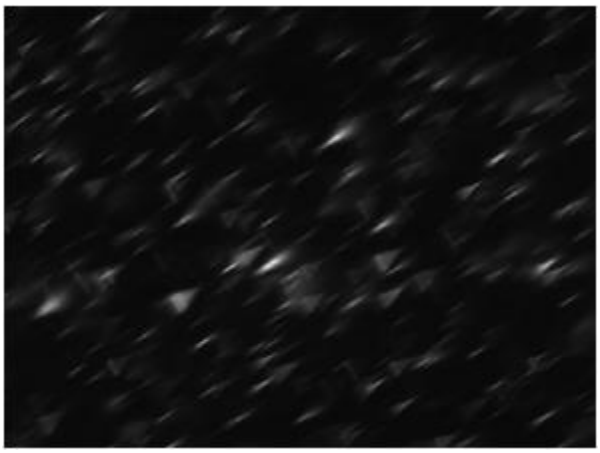

Figure 3.11: Astigmatism caused by refraction in air, acrylic and water[22]

Clearly, these types of images would be inadequate for a 3DPTV application. To correct for this Schmitt (2007) and Grothe (2008) designed, through experimentation and ray-tracing theory, a water-filled prism to bend the light appropriately.[22,29] This prism was fabricated out of acrylic and contained refillable water chambers. The chambers were filled with deionized water via a syringe such that no bubbles formed in the chambers as any air bubbles in the prism would lead to distortion in the resulting image. A general schematic of the ray tracing for the water filled prism can be seen in Figure 3.12.

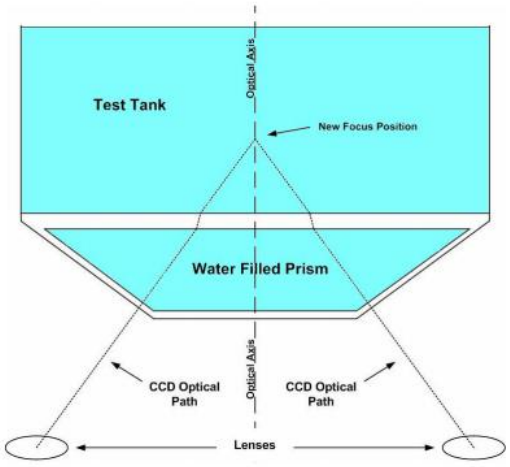


Figure 3.12: Ray tracing showing minimized refraction from water-filled prism[22]

This water-filled prism was placed on the interface of the air and the acrylic top of the tunnel, or the acrylic calibration platform which will be discussed in subsequent sections. Additionally, the platform was secured using aluminum shafts which could be screwed into the lens bracket and fit to the prism's legs. This allowed the location of the water-filled prism to be fixed within a tolerance of approximately 50 microns in each direction. An image of this water-filled prism and aluminum jigs can be seen in Figure 3.13.

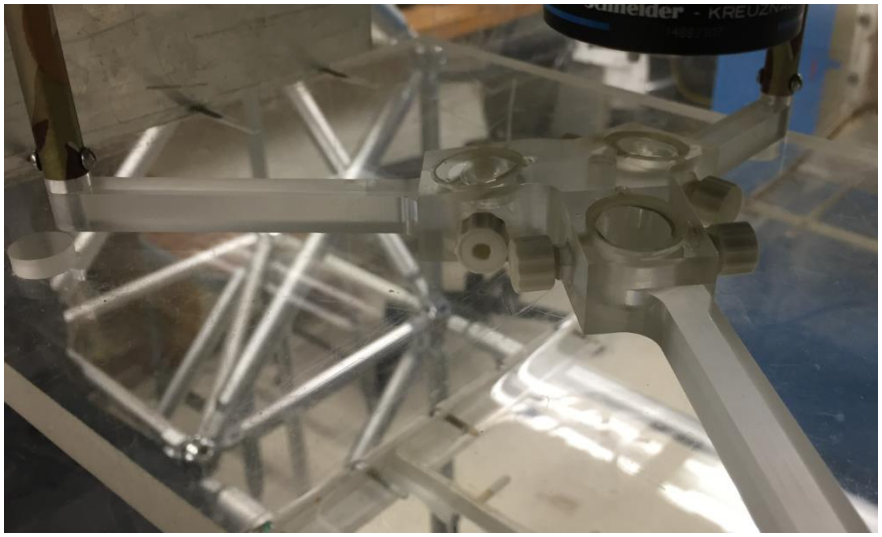

Figure 3.13: Water-filled prism fixed to lens mount assembly

## 3.5 Illumination Source

### *3.5.1 Solo PIV Laser*

To provide proper illumination of the tracer particles in the 3DPTV system, a New Wave Research Solo PIV 120XT dual-pulsed Neodymium-doped Ytrium Aluminum Garnet (Nd:YAG) laser was used. This was capable of providing pulsed illumination which could be appropriately

timed to provide consecutive images with high signal-to-noise ratio. This laser emits visible light at 532 nm wavelength with a maximum energy level of 120 mJ per pulse with a pulse width between 3 and 5 ns. Each beam diameter in this dual laser was 4.5 mm with a divergence of less than 3 mrad. Ideally, each of the two beams from this laser would align on top of each other, but over time internal laser optics may become misaligned. For this reason, the internal optics of the laser were carefully aligned, referencing the Solo PIV user guide, such that the overlap between both beams was maximized.

It is also important to understand that Class IV lasers, such as this, pose significant safety hazards not associated with conventional light. For this reason, LaserShield eyewear with an optical density in wavelengths encompassing 532 nm was 6.5+. Additionally, prior to operation of the laser, the laboratory facility was secured with an appropriately illuminated laser warning light fixed to all entrances. Black laser shrouding material was also used to minimize reflections as the laser entered the flow facility. An image of this laser firing can be seen in Figure 3.14.

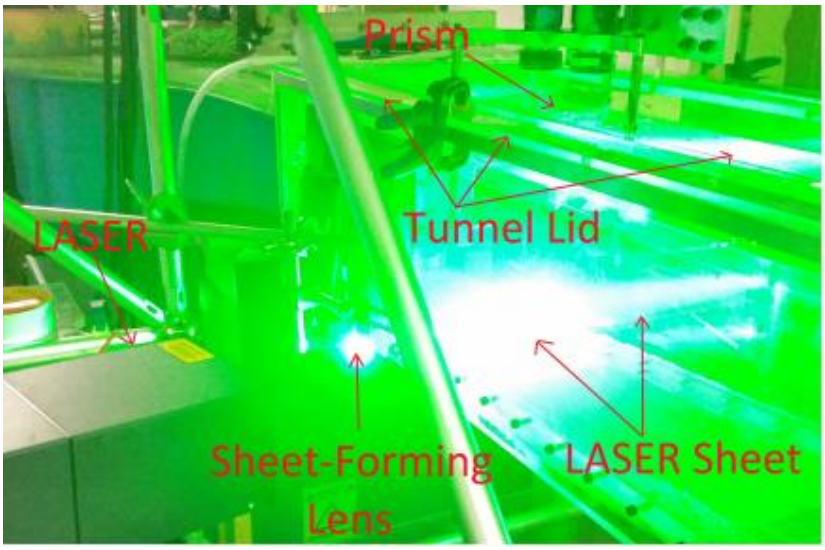


Figure 3.14: Laser sheet formation[3]

### *3.5.2 Laser Sheet Optics*

To appropriately illuminate the VOI, the circular beams coming from the Solo PIV laser needed to be reshaped into a thick flat laser sheet. To do this, a CVI laser Optics 532nm coated, -12.7 mm focal length, plano-concave cylindrical sheet forming laser was used. When appropriately aligned with the circular beam, this lens forms a laser sheet 4.5 mm thick, corresponding to the original diameter of the beam, that spreads along the tunnel's Y-direction to span the entire VOI. Laser reflections from the tunnel's floor caused halo patterns in the particle images, which in turn complicated data reduction. Therefore, additional care was taken to ensure that the laser remained level by using a level and visually inspecting the laser sheet using the proper safety measures. These halos complicated the data reduction and it was necessary to remove them by levelling the laser prior to collecting data. An example of these halos can be seen in Figure 3.15.

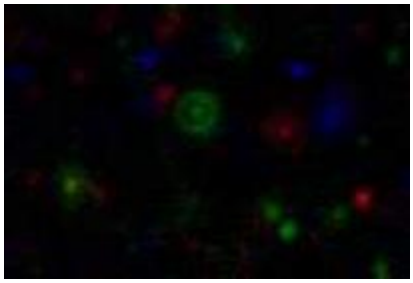

Figure 3.15: Halo illumination of particles caused by laser reflections[3]

## 3.6 Calibration Equipment and Procedure

### *3.6.1 Grid Dot Pattern Target*

In order to appropriately calibrate the 3DPTV system, it was necessary to use a custom built calibration target with an array of distinct dots and grid lines. The dots on the target allowed for distance X,Y,Z coordinated to build a calibration mapping to the x,y camera coordinates.

Furthermore, the grid lines provided a reference for removing camera distortions stemming from misalignment. The process for this calibration and distortion removal is described further in Section 3.6.5.

The primary target used was a 1.59mm thick glass plate with a 40.5mm x 40.5mm regular, repeated laser-etched grid and dot pattern. Holes were also drilled in this plate such that rods could be suspended from the lens assembly. When the plate was appropriately suspended and secured via these rods, a unique dot at the center of the calibration grid was aligned with the camera system's optical center. A schematic of a section of this grid and an image of the unique center dot can be seen in Figure 3.16.

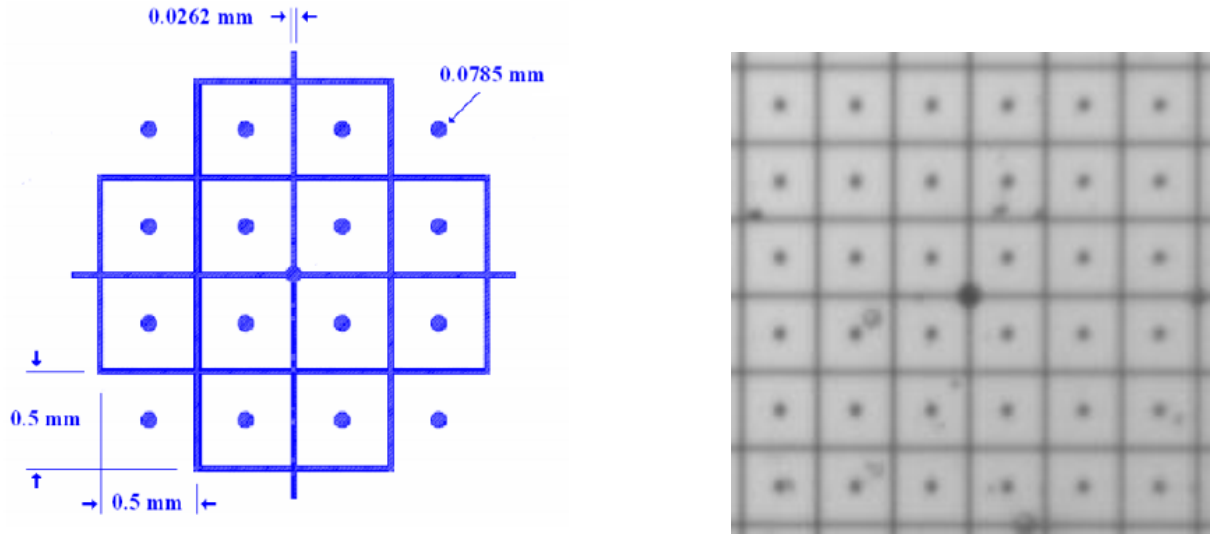


(a) Calibration grid/dot dimensions (b) Section of calibration image

Figure 3.16: Calibration plate dimensions and section of image containing unique center dot[22]

In the grid pattern, each line and dot were place at an interval of 526.2 µm +/- 0.02 µm apart with each line having a thickness of 26.2 um +/- 2um and each dot having a diameter of 78.5 µm +/- 2 µm.

### *3.6.2 Calibration Rigs*

Two calibration rigs were used in the present study. The first was fixed to the lens assembly and used for aligning the three cameras with the optical axis and removing camera distortions. The second was capable of translating through the volume of interest as was necessary to build calibration data.

The first rig was similar to what was used in Grothe (2008). It consisted of six aluminum shafts, the water filled prism, and an acrylic false top designed to fit beneath the water filled prism and mimic the water tunnel top. Three of the shafts were fixed to each of the holes drilled in the calibration target. The shafts were then inserted through holes in the acrylic false top and water filled prism and attached to the second group of three shafts. When complete, the entire assembly was 258.85 mm in height and was fixed to the lens bracket assembly. This allowed the calibration plate to be placed precisely at the focal length of the system, or 536.38 mm along the optical axis from the calibration plate to the CCD. For additional information on how this length was determined see Grothe (2008). This rig can be seen in Figure 3.17 and was used primarily for positioning each CCD correctly with respect to the optical axis and removing camera distortion.

Figure 3.17: Calibration rig with fixed length rods, prism, acrylic platform and calibration plate

The second calibration rig was built and designed in Dona (2015). The rig contained a bar that spanned the Y depth of the flow facility where clamps could be used to secure the entire apparatus in place. A Mitutoyo 0.5 in single-axis linear translation stage with 0.001 in increments was fixed perpendicular to this beam and attached to an L-shaped beam. This L-shaped extension was then attached to an adjustable mount with screws that allowed for the securement of the calibration plate. This assembly allowed for the accurate translation of the calibration plate through entire Z span of the VOI. This assembly was used in conjunction with a custom built platform that simulated the water tunnel top while allowing access to the test section throughout the calibration process. An image of this platform as well as the calibration rig can be seen in Figure 3.18.

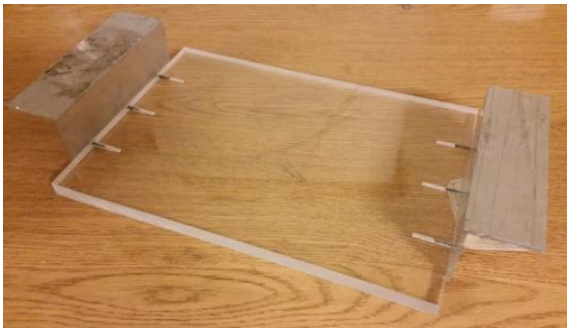

(a) Acrylic calibration platform

(b) Calibration rig with single-axis translation

Figure 3.18: False tunnel top and calibration rig used in the present study[3]

*3.6.3 Calibration Illumination*

To generate adequate calibration images, it was necessary to provide consistent, diffuse backlighting to provide contrast for the lines and dots on the calibration plate. To accomplish this, a simple adjustable neck lamp with a 28W compact fluorescent bulb was used to illuminate a diffuser plate. The power source for this was the standard 120V at 60Hz and 0.44A. This lamp was then placed below a frosted glass diffusor plate to provide sufficiently smooth illumination of the grid target in the VOI. Note that previous studies utilized a Light-Emitting Diode (LED) array to accomplish this, but it was determined that the lamp, when combined with the diffusor plate, provided adequate illumination. An image of this illumination assembly can be seen in Figure 3.19.

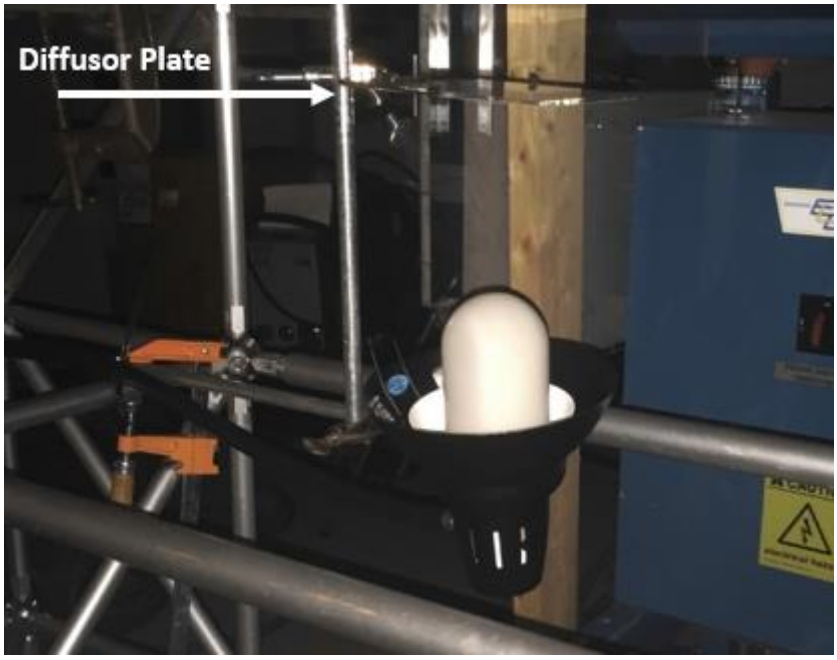


Figure 3.19: Present calibration illumination scheme

*3.6.4 Calibration Procedure*

The first step in the calibration procedure was to fill the water tunnel such that the top of the water was in full contact with the bottom of the calibration platform that was used to simulate the tunnel lid, as was shown in Figure 3.14. Once this water level was confirmed, the platform was removed and the calibration rig shown in 3.13 was attached to the lens bracket assembly. Note that prior to attaching the assembly, each of the three chambers on the water filled prism were filled with a syringe such that no bubbles formed.

Once the assembly was in place, contact between the acrylic false top and the water was confirmed. This ensured that the optical system did not see any of the water's free surface. Next, using the Streams5 software suite from IO Industries, which will be described later in full detail, appropriate lighting of the calibration plate was confirmed. Then, using the translation stages on the 6 stage axis translators, the center dot on the calibration target, as shown in Figure 3.12, was

positioned at the center of each CCD. This was necessary to align the CCDs with the system's optical axis. The next step was to use the rotation stages on the 6 stage axis translators to remove any distortions in each of the three rotational axes of the form shown in Figure 3.20.

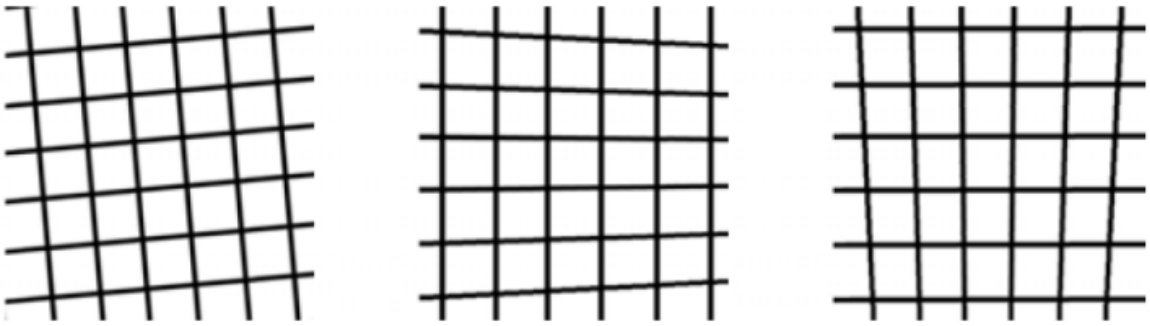

Figure 3.20: Distortion patterns from camera misalignment in each of the three rotational axes[22]

Typically, the in-plane distortion shown in the first grid pattern in Figure 3.16 was most significant and was removed at the center of the CCD first. The distortions at the edges of the CCDs were then removed using rotation through the other axes. This was often an iterative process. Distortions were considered removed when there were no longer distortions along the center and edges of the CCD. The rotation of the CCD to remove these distortions often caused the location of the center dot to move in the CCD. Because of this, the translation stages needed to be used to bring the center dot back to the center of the CCD. Once this was accomplished, it was likely that some distortions would return, so this entire process was performed iteratively.

Once all distortions were removed and the center dot on the calibration target was located at the exact center of each of the CCDs, this calibration rig was removed, and the second calibration rig and platform, shown in Figure 3.14, were installed. An optional triangular piece of tape was then placed onto the grid target to provide a point of reference for the calibration. The

rig was positioned roughly at the bottom of the VOI and a strut was used in combination with a level to ensure that the calibration plate was completely level in all directions. The top span of the calibration rig was set against a metal block set perpendicular to the top of the tunnel. This ensured that the calibration plate was perpendicular to the water tunnel, but was not necessarily completely aligned with the optical system since the optical system was built on a separate scaffolding around the water tunnel. This resulted in apparent in-plane distortions of the calibration grid which needed to be removed for the calibration software to run appropriately. Since distortions had already been removed from the optical system, these distortions were removed to a tolerance of several pixels by carefully adjusting the position of the calibration rig.

Once these distortions were removed, the calibration procedure could commence. The XMV Camera Control Application was used to adjust exposure and gain settings for the cameras and Streams 5 was used for the capture and storage of the images. Ten images were taken at each calibration plane to allow for removal of unwanted background movement. Once images were taken at the bottom of the VOI, the single stage linear axis translator stage was turned one full rotation so that the calibration plate moved up 635 um and calibration images were taken once oscillations damped out and the plate was confirmed to be level. This was accomplished nine more times for a total of 11 calibration planes spanning either side of the VOI. After all images were collected, the building of the calibration Radial Basis Function (RBF) was accomplished using the software suite described in Dona (2015).

## 3.7 Data Acquisition and Experimental Procedure

### *3.7.1 Data Acquisition System Architecture*

The data acquisition system for the present experiment consisted of a single computer with Digital Video Recorder (DVR) hardware, an onboard signal generator, and an external hard disk array. This DVR computer was built by IO industries and contained three DVR Express CLFC Dual-Base boards, each with two Camera Link Cable interfaces. In addition, these boards were linked to the internal signal generator which was necessary in providing precise synchronization between the camera and the laser illumination source. Synchronization with the laser illumination source was accomplished through four BNC outputs, two for the laser's flashlamps and two for the Q-switches. Camera settings, including exposure and gain settings were adjusted using the XMV Camera Control Application. Camera and laser timing were tuned using the DVR express CLFC Control Signal Manager within the Streams 5 software suite. This controlled the master signal generator board, to which the DVR Express and BNC output boards were slaved.[3] A diagram of the complete data acquisition system architecture can be seen in Figure 3.21.

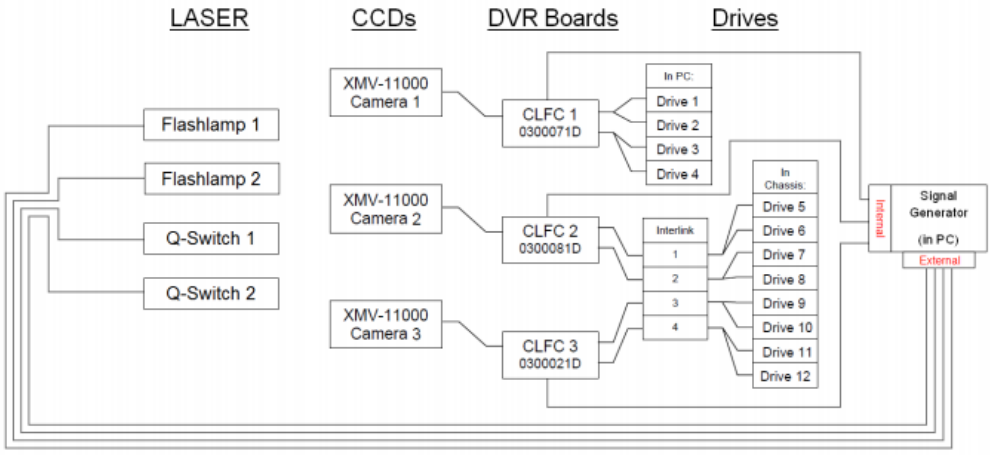


Figure 3.21: Data acquisition equipment control diagram[3]

*3.7.2 Laser Illumination, Alignment, and Timing*

Prior to collecting experimental 3DPTV data, it was necessary to sufficiently align the laser illumination source to the volume of interest. To accomplish this, a laminated index card with markings 13mm above the bottom of the card and 4.5mm thick, corresponding to the dimensions of the VOI, was placed attached to a metal block, so that it stood upright, and placed in the water tunnel. The card and block were then positioned in the center of the cameras' fields of view. This ensured that the card was located at the precise location of the VOI. Next, the laser, described in Section 3.5 was fired at low power. Next, the laser was carefully moved so that the laser sheet, on low power, fell exactly within the markings on the card. After this, the laser was turned to high power, and once again the positioning within the VOI was verified.

Once the laser was aligned with the VOI, it was necessary to configure the laser timing with respect to the camera timing. This was accomplished through the CLFC Control Signal Manager within the Streams 5 software suite. All timing was accomplished with respect to the master trigger on the data acquisition system's internal signal generation board, SG1. This signal was set to 1.9hz at a 50% duty cycle. The three CCDs were then programmed to begin their Triggered Double Exposure (TDE) of 100 ms at the signal's rising edge. This gave an overall camera frame rate of 3.8hz, which is the designed maximum for the CCDs used. Furthermore, since the time between the exposures in this modes was negligible (approx. 800 ns) compared to the 0.6 ms delta t desired in the present study, it was not considered in the timing of laser pulses. The first laser pulse was timed to begin at $0.5*\Delta t$ prior to the end of the first exposure, and the second laser was timed to begin at $0.5* \Delta t$ after the end of the first exposure. Additionally, to optimize the energy per laser pulse, the flashlamp was triggered 190 um prior to firing the laser

Q-switch. Also, it is worth noting that the duration of each laser pulse was between 3 and 5 ns. A diagram of this timing scheme can be seen in Figure 3.22.

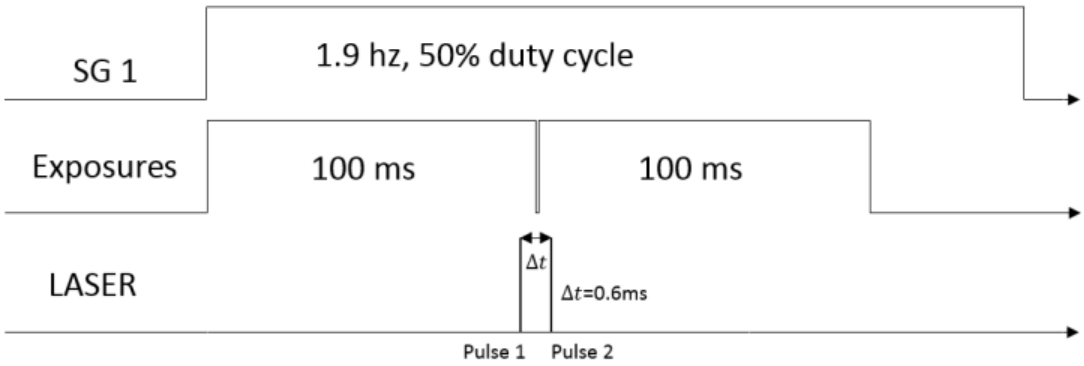


Figure 3.22: Laser and camera timing diagram[3]

For the present deltat of 0.6ms this meant that the flashlamp and Q-switch for laser 1 were delayed from SG1 by 99.51 ms and 99.70 ms respectively, and the flashlamp and Q-switch for laser 2 were delayed from SG1 by 100.11 ms and 100.30 ms respectively.

### *3.7.3 Particle Selection and Seeding*

Particle selection for the present study was accomplished by Dona (2015). Information considered when selecting the appropriate particle included particle diameter, specific gravity, imaged size, imaged intensity, and response time. These properties allowed for the evaluation of the non-dimensional Stokes Number, Reynolds number, and volume fractions for each particle. Ultimately, these numbers give the researcher an idea for how many particles can be seeded into the flow before running into multiphase flow limits.

The particles selected to be used in this study were Rutile $TiO_2$ < 5 um diameter particles. Particle seeding was accomplished by creating a solution of approximately 1.00g of these particles in 0.25L of water. This solution was then divided into the three particle seeding bottles described in Section 3.1.3. A schematic of where these particles were seeded with respect to the backward-facing step can be seen in Figure 3.23 below.

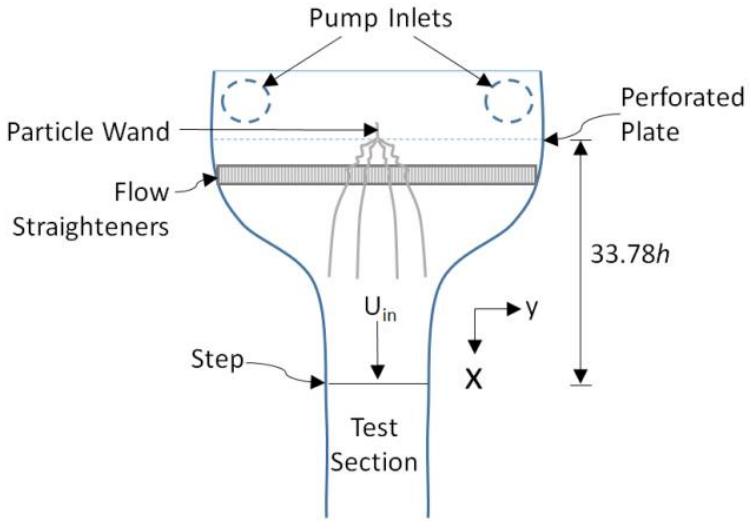


Figure 3.23: Particle Seeding Diagram[3]

*3.7.4 Experimental Procedure*

Once the appropriate camera alignment, calibration procedure, laser alignment, laser timing, and particle preparation were accomplished, data were ready to be collected. To collect data, the flow facility pumps were set to 341 RPM providing an inflow velocity of 22 cm/s. Once the RPMs were steady, the particle solutions of Rutile $TiO_2$ particles were connected to the siphon system. The siphon was initiated by simply squeezing each of the seeding bottles. Once

the siphon began, the CCDs were placed in live and typically set to record 200 images. As the CCDs recorded, the laser was switched to high power and timing was set to external mode. Once all lights in the laboratory were turned off, the laser aperture was opened and the lasers were fired. If all timing was correct this resulted in image pairs with illuminated particles at the desired $\Delta t$.

# Chapter 4

# RESULTS AND DISCUSSION

In the present chapter, results from the Three-Dimensional Particle Tracking Velocimetry (3DPTV) system are presented. An evaluation of the LES models outlined in Chapter 2 is also presented. Additionally, an uncertainty analysis of the velocity vector fields and turbulence is offered. In the present study, a method for increasing particle density, and thus vector density, was developed, but is not fully established, and thus the 3DPTV velocity results presented in this chapter were obtained from data sets produced by Dona (2015).

## 4.1 3DPTV Results

In Dona 2015, unstructured 3DPTV 3D3C vector fields were experimentally gathered on the backward-facing step for a total of six fields to obtain statistical convergence. The number of vectors in the volume of interest, whose dimensions are presented in chapter 3, for each of these fields varied from 20,000 to 25,000. Note that these vector fields were reduced to a Z-dimension range that maximized vector density and resulted in dimensions for the vector field are slightly different than those for the VOI (3.3mm as opposed to 4.5mm). An example of one of these fields, magnified to show flow details, can be seen in Figure 4.1.

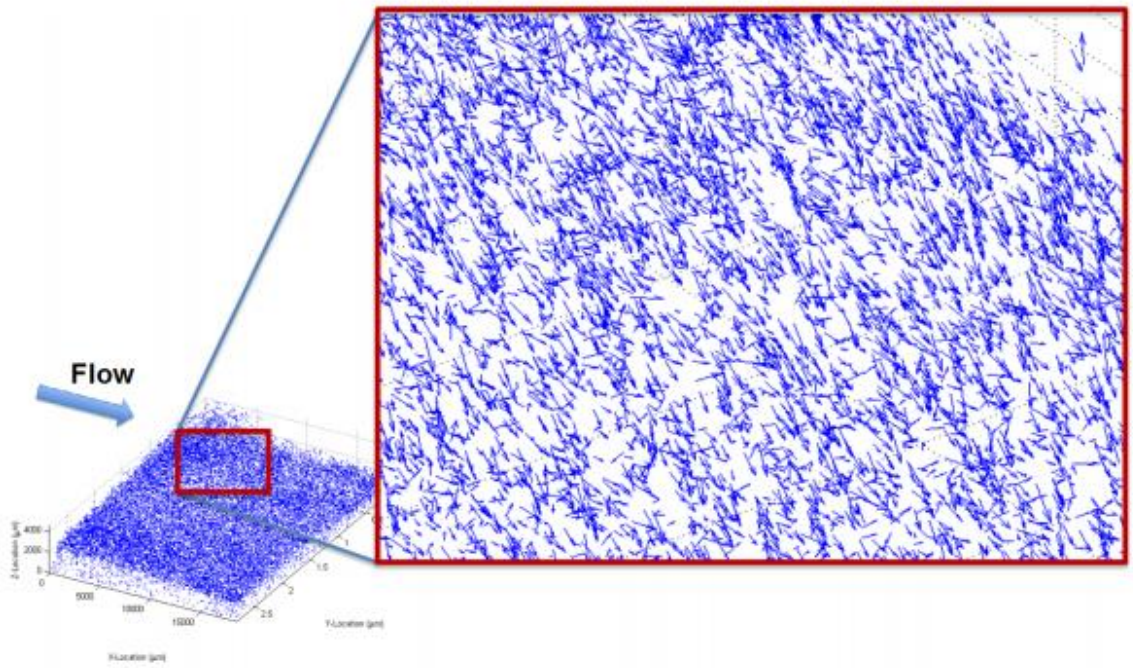


Figure 4.1: 3DPTV 3D3C vector field for a volume of approximately 30mm x 20mm x 3.3mm$^3$

These unstructured grids were then interpolated, using a three-dimensional ellipsoidal interpolation scheme developed by Talapatra and Katz for a similar purpose, onto a structured grid.[3,31] This three-dimensional structured grid had a spacing of 300$\mu$m and resulted in approximately 163,000 grid locations. An image of the interpolated vector field can be seen in Figure 4.1.

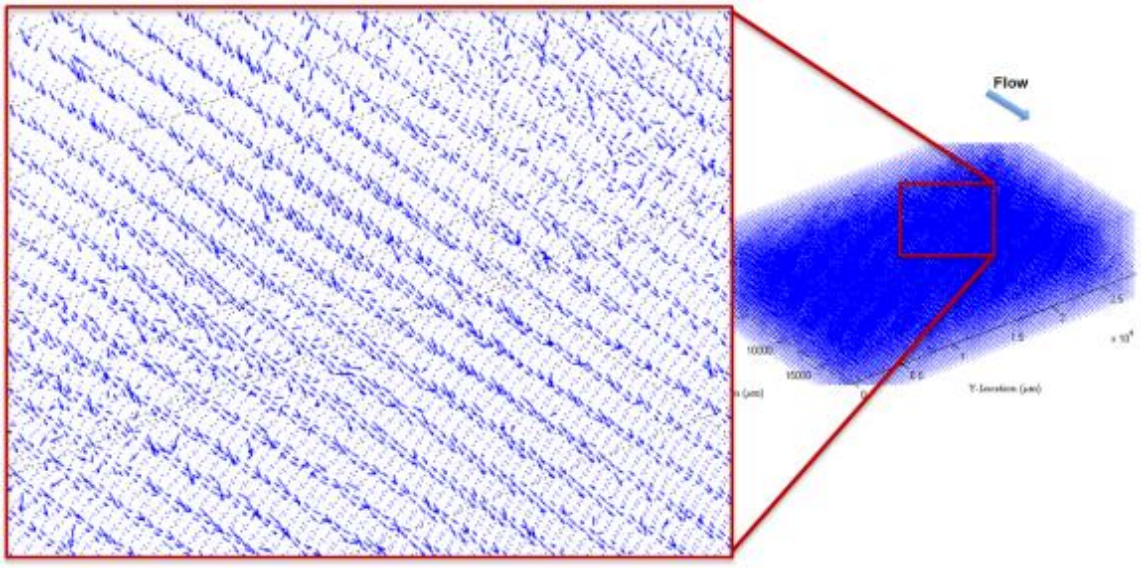


Figure 4.2: 3DPTV results in 3D3C structured velocity field with grid spacing of 300$\mu$m[3]

To get a better idea of the flow structure, the vorticity of the velocity field was also computed. This was accomplished by simply taking the geometric curl of the velocity field, and was best viewed as contours of constant vorticity. To show the general structure of the flow in the XZ-plane, the vorticity component in the Y-direction ($\omega_{xz} = \frac{\partial u_x}{\partial z} - \frac{\partial u_z}{\partial x}$) was extracted, an ensemble average was performed, and the constant vorticity contours were plotted. This can be seen in Figure 4.3. Note that in this Figure, flow was along the positive X-axis.

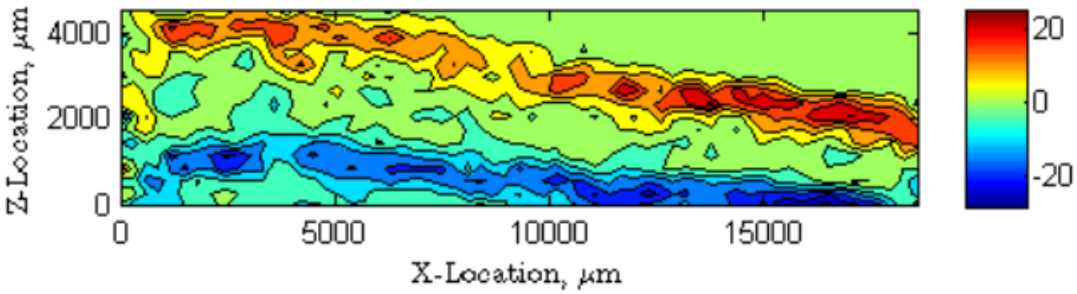


Figure 4.3: Contours of mean vorticity ($s^{-1}$) component normal to Y-axis[3]

Notice in this plot, that the mean vorticity increases in magnitude as the flow propagates downstream; however, the vorticity values in each of the vorticity sheets seen in Figure 4.3 were within three times the characteristic vorticity of the incoming flow over the backward-facing step.[3] In addition to visualizing the flow field with vorticity contours, Dona conducted a complete uncertainty analysis of the experimental velocity field. For details on the uncertainty of the velocity fields, see Dona (2015).

### 4.2 Evaluation of SGS Stress Models

The velocity vector fields, described in Section 4.1, were filtered using Equation 2.5 and the Smagorinsky, Similarity, Mixed, Dynamic, Coherent Structures, and Stretched Vortex Models were applied to the filtered velocity field. This velocity filtering was done at a variety of different levels relative to the fine resolution scale, $\delta$, obtained in the experimental vector fields; however, the results presented in this section are for an LES filtering scale of $\Delta=5\delta$ unless otherwise specified.

The *a priori* test conducted on the models directly compared the modeled SGS stress tensor elements, $\tau_{ij}^{\Delta,\mathrm{mod}}$, with the experimental SGS stress elements calculated using Equation 2.8. In addition to obtaining a simple correlation coefficient between the modeled and actual SGS stress, the correlation between the actual SGS dissipation or transfer of kinetic energy, $-\tau_{ij}^{\Delta}\tilde{S}_{ij}$, and the modeled SGS dissipation $-\tau_{ij}^{\Delta,\mathrm{mod}}\tilde{S}_{ij}$ was also determined. The correlation coefficients calculated were Pearson Correlation Coefficients. For details on the calculation of these coefficients, see Dona (2015).

*4.2.1 SGS Stress Contours and Correlations*

Since the SGS stress tensor, $\tau_{ij}^{\Delta}$, is a second-order tensor in three dimensional space, it is difficult to visualize all nine elements of the tensor. For this reason, only contours of the *XY* stress tensor element, $\tau_{12}^{\Delta}$, are presented in this section. Note that, while this only represents a single tensor element in a single plane, three-dimensional data for each of the deviatoric stress components, $\tau_{12}^{\Delta}$, $\tau_{23}^{\Delta}$, and $\tau_{13}^{\Delta}$ are also available. For comparison, the experimentally calculated SGS stress tensor in the *XY* direction is presented in Figure 4.4.

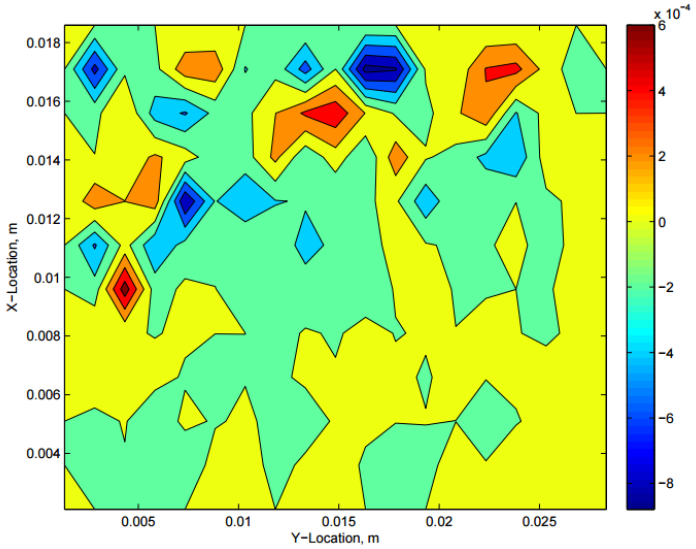


Figure 4.4: Experimentally calculated SGS stress tensor element, $\tau_{12}^{\Delta}$. Units are in $m^2/s^2$.

Contours of the same *XY* SGS stress tensor element for the Smagorinsky, Similarity, Coherent Structures, Mixed, Dynamic, and Stretched Vortex models can be seen in Figure 4.5.

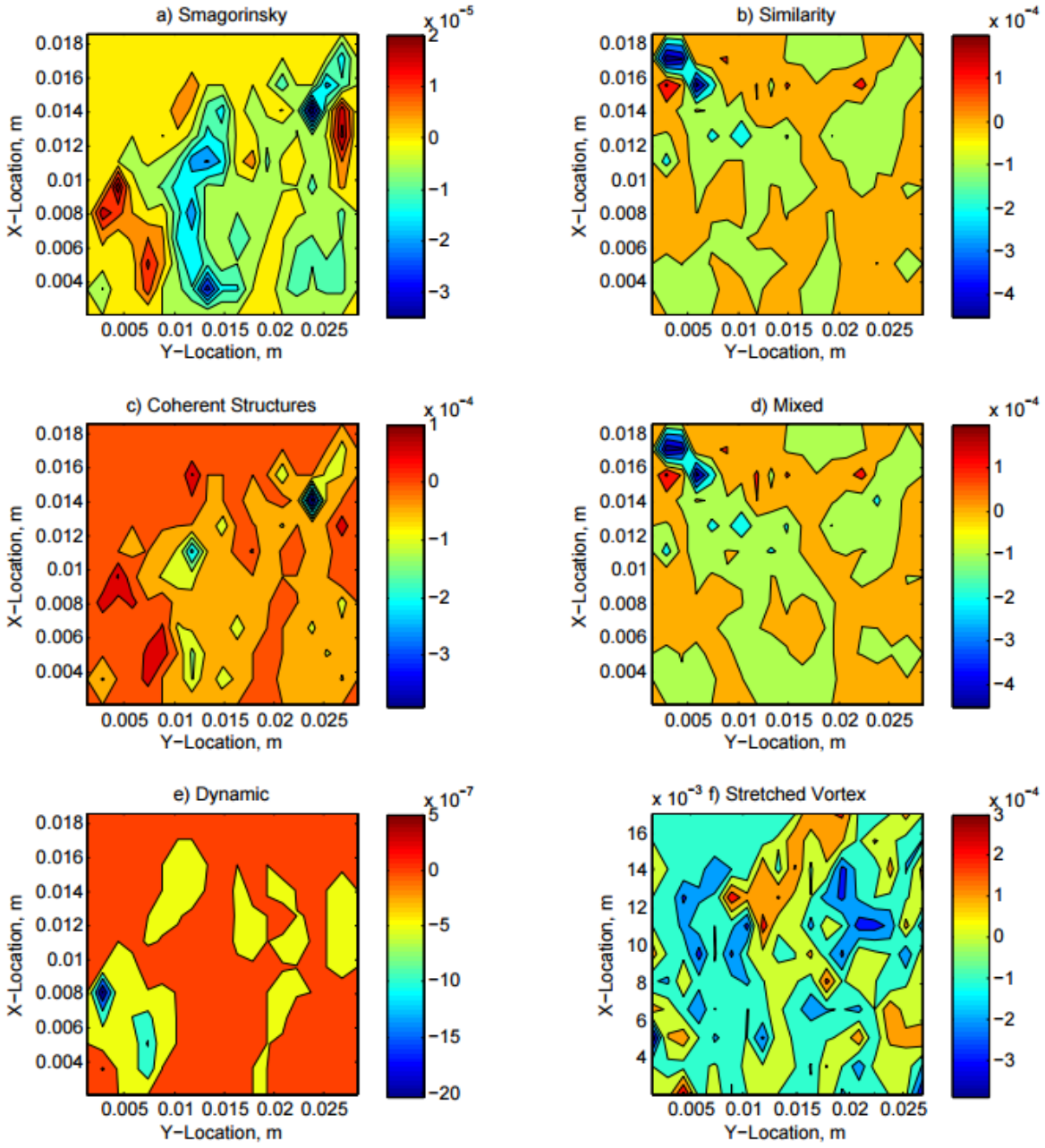


Figure 4.5: LES SGS modeled *XY* SGS stress tensor elements. Note that flow direction is from top to bottom and that units are in $m^2/s^2$.

Comparing the LES models in Figure 4.5 to the experimentally calculated SGS stress in Figure 4.4, the Similarity and Mixed Models most closely model subgrid-scale stress. Also note the

comparable these two models to each other. This is the case because they are essentially the same models with the Mixed model simply incorporating the Smagorinsky model into the Similarity model. These results agree with the work of Liu, as presented in KM (2000), where the Similarity and Mixed Models SGS stress contours were nearly identical to one another and showed the highest correlation to the experimental data.[7] The dynamic model has very little correlation to the experimental while the Smagorinsky, Coherent Structures, and Stretched Vortex models do slightly better; however, in each of these models, regions of high SGS stress appear random when compared to regions of high SGS stress in the experimental data. Note that KM also documented little commonality between the Smagorinsky model's contours and the experimental data.

The above observations are also confirmed with the numerical correlation coefficients. Statistics were collected on six velocity fields so that the Pearson Correlation Coefficients converged. The process of collecting statistics and implementing the Pearson Correlation Coefficients is described in Dona (2015). The results for the correlation between the SGS stress tensor elements for the various models and the experimentally calculated SGS stress tensor can be seen in Table 4.1:

Table 4.1: Correlation coefficients of modeled deviatoric stress tensor elements.

| **Model Type** | $\tau_{12}^{\Delta}$ | $\tau_{13}^{\Delta}$ | $\tau_{23}^{\Delta}$ |
|---|---|---|---|
| Smagorinsky Model | 0.0497 | 0.0118 | 0.0288 |
| Similarity Model, *γ=1* | 0.5553 | 0.5174 | 0.5379 |
| Similarity Model, *γ=2* | 0.4310 | 0.3552 | 0.3768 |
| Mixed Model, *γ=1* | 0.5554 | 0.5170 | 0.5377 |
| Mixed Model, *γ=2* | 0.4310 | 0.3543 | 0.3764 |
| Dynamic Model, α=1 | -0.0238 | -0.0502 | -0.0152 |
| Dynamic Model, α=2 | -0.0431 | 0.0045 | 0.0135 |
| Coherent Structures Model | 0.0490 | 0.0126 | 0.0135 |
| Stretched Vortex Model | 0.0062 | -0.0373 | 0.0022 |

Notice that the values for the Smagorinsky Model fall in the expected range of 0~0.2.[7] The Similarity and Mixed models both had relatively high correlation coefficients (between 0.3 and 0.6) and were similar to each other as noted by KM. Notice also that the Dynamic, Coherent Structures, and Stretched Vortex models did not perform well. In Dona, it is hypothesized that the complexity of the flow may have led to negative correlation coefficients for the Dynamic Model and more data points in the *Y* direction may be required in order to achieve stable Dynamic Smagorinsky coefficients values. The reason behind the low correlation coefficients of the CSM and SVM is unclear, but may also have to do with the complexity of the flow. This was surprising, particularly for the SVM since, like the model, the flow is vortical in nature.

### *4.2.2 SGS Dissipation Contours and Correlations*

The experimental local SGS dissipation, $-\tau_{ij}^{\Delta}\tilde{S}_{ij}$, contours in the same *XY* plane as Figures 4.4 and 4.5 can be seen in Figure 4.6.

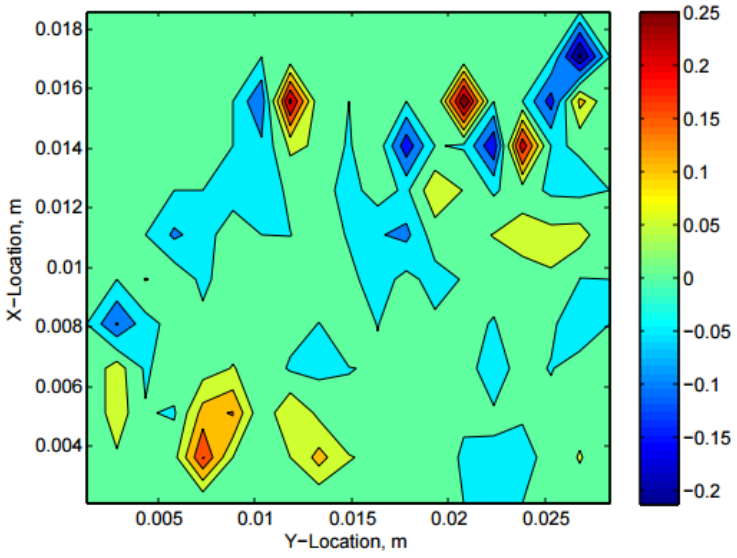


Figure 4.6: Experimentally calculated SGS energy dissipation, $-\tau_{ij}^{\Delta}\tilde{S}_{ij}$. Note that units are in $m^2/s^3$ and flow direction is from top-to-bottom

Contours of the same *XY* SGS energy dissipation for the Smagorinsky, Similarity, Coherent Structures, Mixed, Dynamic, and Stretched Vortex models can be seen in Figure 4.7.

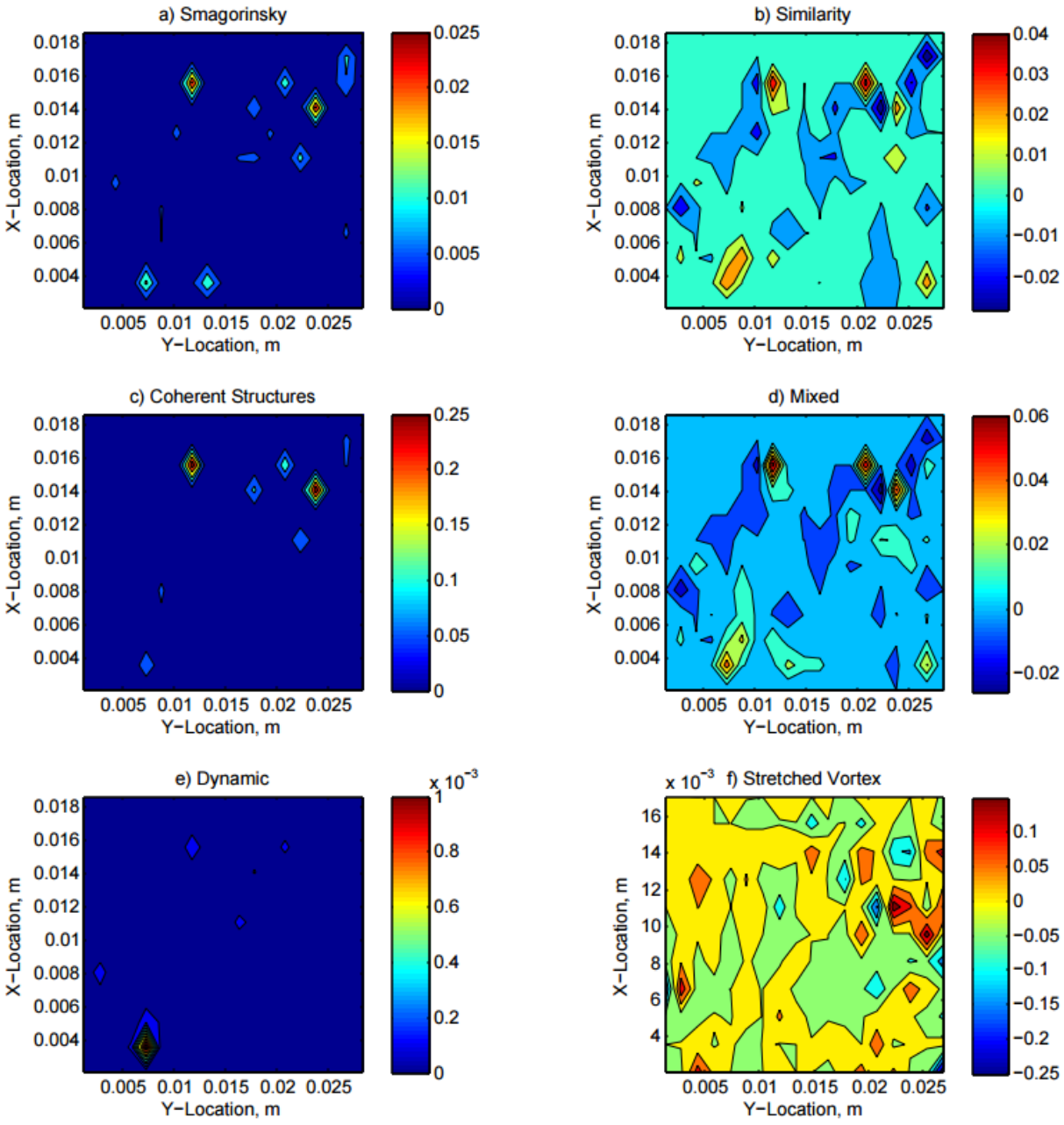


Figure 4.7: LES SGS modeled *XY* SGS energy dissipation contours. Note that flow direction is from top to bottom and that units are in $m^2/s^3$.

Notice that some of these plots show a significant amount of negative values for the SGS energy dissipation. This is known as the energy backscatter. This backscatter has been observed in past studies, primarily by Piomelli (1991) and Liu (1994).[20,32] Notice also that the Smagorinsky, Coherent Structures, and Dynamic models show no backscatter indicating that they are purely dissipative models. The lack of taking this local backscatter into account it one of the key limitations of models using the eddy viscosity hypothesis. Since backscatter is a natural phenomenon, this is an undesirable attribute of such eddy viscosity models and contributes to its lower correlation coefficients.

Aside from the backscatter, the SGS energy dissipation for the individual LES models compare with the experimental results in a similar manner to the SGS stress contours. For example, the Similarity and Mixed Models closely match the experimental contours. On the other hand, the Smagorinsky, Dynamic, Coherent Structures, and Stretched Vortex Models do not closely match the experimentally calculated dissipation and therefore exhibit low correlation. Notice that the Smagorinsky, Coherent Structures, and Dynamic models do exhibit similar contour patterns. This is likely due to the fact that each of these models are forms of the eddy-viscosity model. The correlation coefficients for the dissipation of the various models can be seen in Table 4.2:

Table 4.2: Correlation of LES models' SGS dissipation to experimental dissipation

| **Model Type** | **Correlation** |
|---|---|
| Smagorinsky Model | 0.1123 |
| Similarity Model, *γ=1* | 0.8645 |
| Similarity Model, *γ=2* | 0.8088 |
| Mixed Model, *γ=1* | 0.7886 |
| Mixed Model, *γ=2* | 0.7936 |
| Dynamic Model, α=1 | -0.1358 |
| Dynamic Model, α=2 | -0.0466 |
| Coherent Structures Model | 0.0840 |
| Stretched Vortex Model | 0.0051 |

From this table, it is clear to see that, while the Smagorinsky model did have very high correlation coefficients, it did not result in adequate levels of dissipation when combined with the Similarity model to form the Mixed Model. Notice that the correlation coefficients follow a similar trend between the models as was seen with the SGS stress.

### *4.2.3 SGS Force Correlation*

In addition to the SGS stress and dissipation, the correlation of the SGS force, $\nabla \cdot \tau^{\Delta}$, or simply the divergence of the SGS stress was also considered. The results of this correlation can be seen in Table 4.3:

Table 4.3: Correlation of LES models' SGS force to experimental SGS force

| **Model Type** | **Correlation** |
|---|---|
| Smagorinsky Model | -0.0055 |
| Similarity Model, *γ=1* | 0.4805 |
| Similarity Model, *γ=2* | 0.4384 |
| Mixed Model, *γ=1* | 0.4795 |
| Mixed Model, *γ=2* | 0.4367 |
| Dynamic Model, α=1 | -0.1924 |
| Dynamic Model, α=2 | -0.0932 |
| Coherent Structures Model | 0.0005 |
| Stretched Vortex Model | -0.0788 |

As in the previous cases, the SGS force correlation is highest for the Similarity and Mixed Models (0.4~0.5). Notice also that the correlations for the Smagorinsky, Dynamic, and CSM models are very small indicating little or no correlation between the modeled and experimental SGS force.

## 4.3 Uncertainty Analysis

### *4.3.1 Uncertainty of the Velocity*

An uncertainty analysis for the 3DPTV system was conducted by Dona 2015. This analysis was performed to characterize the uncertainty associated with experimental position and displacement error arising from instrumentation error. To evaluate the accuracy of the SGS stresses for the various LES models in the previous section, it is necessary to assess how this error propagates through the equations for the LES models. To do this, the traditional approach for the propagation of uncertainties presented in Taylor (1982) was used.[33] This approach states that the uncertainty of any function, $q$, with variables $x,\ldots z,$ who have measured uncertainties associated with them of $\delta x,\ldots \delta z,$ is given by Equation 4.1:

$$\delta q = \sqrt{\left(\frac{\partial q}{\partial x}\delta x\right)^2 + \cdots + \left(\frac{\partial q}{\partial z}\delta z\right)^2}. \tag{4.1}$$

Following this formulation, the uncertainty for the velocity in the x-direction, $u = \Delta x/\Delta t$, is then given by Equation 4.2:

$$\delta u = \sqrt{\left(\frac{\partial u}{\partial \Delta x}\delta \Delta x\right)^2 + \left(\frac{\partial u}{\partial \Delta t}\delta \Delta t\right)^2} \approx \sqrt{\left(\frac{1}{\Delta t}\delta \Delta x\right)^2}. \tag{4.2}$$

Note that $\delta\Delta t$ has been ignored in this equation because the error associated with the time-step is considered negligible when compared to position and displacement error. In this equation, $\delta\Delta x$ represents the displacement error in the x-direction. This can easily be extrapolated to the y and z

dimensions for the *v* and *w* velocities. The displacement error in the y and z directions is simply given by $\delta\Delta z$ and $\delta\Delta z$ respectively. Using Equation 4.1, these displacement errors can be recast in terms of position errors. For example, the error for the displacement $\Delta x = x_2 - x_1$ can be written as Equation 4.3,

$$\delta\Delta x = \sqrt{\left(\frac{\partial\Delta x}{\partial x_2}\delta x_2\right)^2 + \left(\frac{\partial\Delta x}{\partial x_1}\delta x_1\right)^2} = \sqrt{(1 * \delta x_2)^2 + (-1 * \delta x_1)^2}. \qquad (4.3)$$

Now, if the position error at point one, $\delta x_1$, is the same as the position error at point two, $\delta x_2$ (i.e. $\delta x_1 = \delta x_2$), then Equation 4.3 simplifies to $\delta\Delta x = \delta x\sqrt{2}$ where $\delta x$ is simply the position error associated with either $x_1$or $x_2$. This results in a final expression for the uncertainty associated with the velocity in the x-direction as given in Equation 4.4:

$$\delta u = \sqrt{\left(\frac{1}{\Delta t}\delta\Delta x\right)^2} = \sqrt{\left(\frac{\sqrt{2}}{\Delta t}\delta x\right)^2}. \qquad (4.4)$$

This can naturally be extrapolated to the *v* and *w* velocities. In Dona (2015), the position errors in the x and y (in-plane) directions were both less than 0.05% of the full-scale and the position error in the z (out-of-plane) direction was 0.25% of the full scale. This corresponds to an in-plane uncertainty of 0.163$\mu$m and an out-of-plane uncertainty of 0.813$\mu$m. Now, after applying Equation 4.4 and the 0.6 ms $\Delta t$ used in the study, it was determined that the uncertainty of the unfiltered velocity field, originating in the position error, was 383$\mu$m/s for velocity in the x-direction, 383$\mu$m/s for the velocity in the y-direction, and 1915$\mu$m/s in the z-direction . These uncertainties correspond to 0.17% and 0.87% of the freestream velocity in the in-plane and out-of-plane directions respectively and thus the uncertainty of the velocity field was low enough as to have a negligible impact on the results.

*4.3.2 Uncertainty of the Filtered Velocity*

Since the LES models rely on the filtering of the velocity field via Equation 2.5, it is necessary to carry the error propagation through this integral. The final form of the LES filter is given in Equation 4.5 below.

$$\tilde{\boldsymbol{u}}(\boldsymbol{x},t) = \int \left(\frac{6}{\pi\Delta^2}\right)^{3/2} \exp(-6r^2/\Delta^2)\boldsymbol{u}(\boldsymbol{x}-\boldsymbol{r},t)d\boldsymbol{r}. \tag{4.5}$$

Note that since the radius of the Gaussian filter, *r*, is integrated away in the above expression and $\Delta$ refers to a fixed LES filter size, it follows that $\tilde{\boldsymbol{u}}(\boldsymbol{x},t) = f(\boldsymbol{u})$, or that the filtered velocity's only functionality is with $\boldsymbol{u}$. Using this and Equation 4.1, the expression for the uncertainty of the filtered velocity becomes:

$$\delta\tilde{\boldsymbol{u}} = \sqrt{\left(\frac{\partial\tilde{\boldsymbol{u}}}{\partial\boldsymbol{u}}\delta\boldsymbol{u}\right)^2}\text{, where} \tag{4.6a}$$

$$\frac{\partial\tilde{\boldsymbol{u}}}{\partial\boldsymbol{u}} = \int \left(\frac{6}{\pi\Delta^2}\right)^{3/2} \exp(-6r^2/\Delta^2)\, d\boldsymbol{r} \tag{4.6b}$$

Note that in Equation 4.6a, $\delta\boldsymbol{u}$ refers to the uncertainty associated with the unfiltered velocity as calculated in the above section as $\delta u = \frac{\sqrt{2}}{\Delta t}\delta x$. In Equation 4.6b, $r^2 = r_1^2 + r_2^2 + r_3^2$ and since this equation is over an infinite domain, the integral of the Gaussian becomes $\left(\frac{\pi}{6/\Delta^2}\right)^{3/2}$. Using this, the final expression for the uncertainty of the filtered velocity is then given by:

$$\delta\tilde{\boldsymbol{u}} = \sqrt{\left(\left(\frac{6}{\pi\Delta^2}\right)^{3/2}\left(\frac{\pi}{6/\Delta^2}\right)^{3/2}\delta\boldsymbol{u}\right)^2} = \sqrt{(1\cdot\delta\boldsymbol{u})^2} = \delta\boldsymbol{u}. \tag{4.7}$$

Notice that this implies that for any given LES filter size $\Delta$, the uncertainty associated with the filtered velocity is identical to the uncertainty associated with the unfiltered velocity. This means that the uncertainty associated with the filtered velocity in the present experiment was 383$\mu$m/s

(0.17% of the freestream) for the in-plane filtered velocity and 1915$\mu$m/s (0.87% of the freestream) for the out-of-plane filtered velocity.

### *4.3.3 Uncertainty of the Various LES Models*

To assess the uncertainty of the LES SGS stress contours presented in this chapter, it is necessary to propagate the uncertainty associated with this filtered velocity through each of the individual models. Since these models rely on the filtered rate of strain tensor, $\tilde{S}_{ij}$, as given in Equation 2.11 it is necessary to calculate its associated uncertainty. The filtered rate of strain tensor relies on taking spatial partial derivatives of the filtered velocity, which in the application of LES are finite differences between the velocity at different points along the LES grid. This means that the filtered rate of strain is effectively calculated through Equation 4.8:

$$\tilde{S}_{ij} = \frac{1}{2}\left(\frac{\Delta\tilde{u}_i}{\Delta x_j} + \frac{\Delta\tilde{u}_j}{\Delta x_i}\right). \tag{4.8}$$

In this expression, $\Delta\tilde{u}_i$ is simply the difference of the filtered velocity between two points, meaning its uncertainty is $\delta\Delta\tilde{\boldsymbol{u}} = \delta\tilde{\boldsymbol{u}}\sqrt{2}$, just as was demonstrated for the displacement error in Equation 4.3. Additionally, the $\Delta x_j, \Delta x_i$ terms in Equation 4.8 refer to the finite filtered grid spacing and therefore are the same in all directions and do not have uncertainty associated with them. After applying this and the fact that the uncertainty associated with the filtered velocity is the same as the uncertainty associated with the unfiltered velocity to Equation 4.1, the expression for the uncertainty of the filtered rate of strain tensor becomes:

$$\delta\tilde{S}_{ij} = \sqrt{\left(\frac{\sqrt{2}\delta u_i}{2\Delta x_j}\right)^2 + \left(\frac{\sqrt{2}\delta u_j}{2\Delta x_i}\right)^2} \tag{4.9}$$

Since the grid spacing is the same in all directions and the maximum velocity uncertainty is in the out-of-plane direction (i.e. the 3 direction), then the maximum uncertainty for the filtered rate of strain tensor is in the 33 direction. A contour plot of this uncertainty as a percentage of the actual filtered rate of strain tensor for a single *Z*-slice for a single velocity field is shown in Figure 4.8.

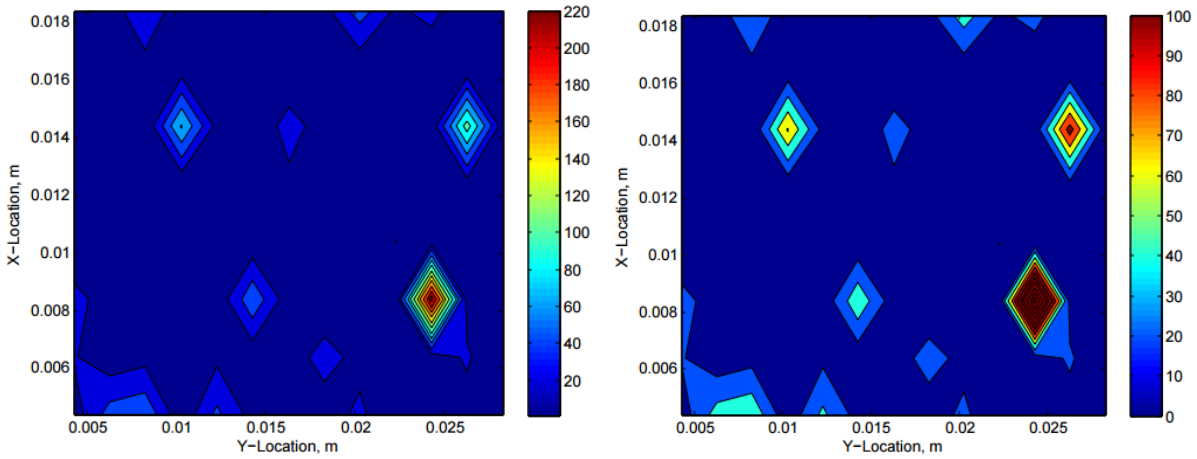


(a) No axis scaling (b) Axis scaled for 0-100%

Figure 4.8: Uncertainty of $\delta\tilde{S}_{33}$ as a percentage of $\tilde{S}_{33}$

Notice in this Figure 4.8(a) that there is one region of high (above 200%) uncertainty. This is likely due to the actual value of the filtered rate of strain being very low at this location. The mean uncertainty for this region is 34%, a value likely to be skewed by the small regions of very high uncertainty. In Figure 4.8(b), it is clear to see the for much of the slice, the uncertainty is below 10% with some areas of uncertainty in the 30-40% range.

With the uncertainty of the filtered rate of strain tensor calculated, it is possible to determine the uncertainty associated with the Smagorinsky model. In its final form, the Smagorinsky model is given as $\tau_{ij}^{\Delta,\text{smag}} = -2(C_S\Delta)^2\sqrt{2\tilde{S}_{ij}\tilde{S}_{ij}}\tilde{S}_{ij}$. Since the only variable in this

expression with uncertainty associated with it is $\tilde{S}_{ij}$, the uncertainty associated with the Smagorinsky model can be given as:

$$\tau_{ij}^{\Delta,\text{smag}} = \sqrt{\left(\frac{\partial \tau_{ij}^{\Delta,\text{smag}}}{\partial\, \tilde{S}_{ij}}\, \delta\tilde{S}_{ij}\right)^2}\text{, where} \tag{4.10a}$$

$$\frac{\partial \tau_{ij}^{\Delta,\text{smag}}}{\partial\, \tilde{S}_{ij}} = -2(C_S\Delta)^2\left[2\left(2\tilde{S}_{ij}\tilde{S}_{ij}\right)^{-1/2}\tilde{S}_{ij}\tilde{S}_{ij} + \sqrt{2\tilde{S}_{ij}\tilde{S}_{ij}}\right] \tag{4.10b}$$

The uncertainty of the modeled SGS stress as a percentage of the modeled stress for a single *Z*-slice for a single velocity field in the 33 direction, $\tau_{33}^{\Delta,\text{smag}}$, can be seen in Figure 4.9.

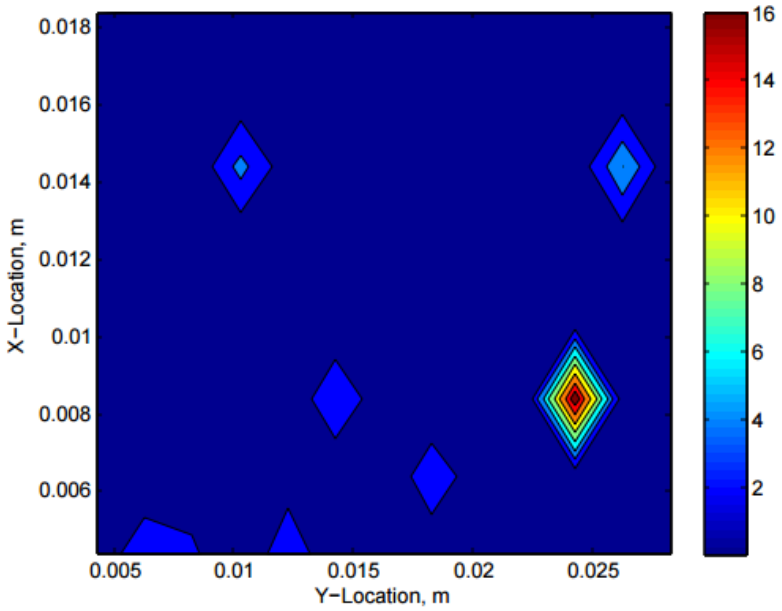


Figure 4.9: Uncertainty of $\delta\tau_{33}^{\Delta,\text{smag}}$ as a percentage of $\tau_{33}^{\Delta,\text{smag}}$

Notice that there is still a region of higher uncertainty located at approximately *X*=0.008 and *Y*=0.025, but, at less than 20%, this uncertainty is lower than the uncertainty associated with the filtered rate of strain tensor at the same location.

The next model to assess the uncertainty of is the Similarity Model. Recall that the Similarity Model in its final form is given as, $\tau_{ij}^{\Delta,\mathrm{sim}} = C_{\mathrm{sim}}\left(\overline{\widetilde{u}_i\widetilde{u}_j} - \overline{\bar{u}}_i\overline{\bar{u}}_j\right)$. In this model, there are two terms that have an associated uncertainty, $\overline{\bar{u}}_i$and $\overline{\widetilde{u}_i\widetilde{u}_j}$. Furthermore, for the present study, $C_{\mathrm{sim}}$=1. From this the total expression for the uncertainty for the Similarity model is given as:

$$\delta\tau_{ij}^{\Delta,\mathrm{sim}} = \sqrt{\left(\frac{\partial\tau_{ij}^{\Delta,\mathrm{sim}}}{\partial\,\overline{\widetilde{u}_i\widetilde{u}_j}}\,\delta\overline{\widetilde{u}_i\widetilde{u}_j}\right)^2 + \left(\frac{\partial\tau_{ij}^{\Delta,\mathrm{sim}}}{\partial\overline{\bar{u}}_i}\,\delta\overline{\bar{u}}_i\right)^2}\text{, where} \qquad (4.11a)$$

$$\frac{\partial\tau_{ij}^{\Delta,\mathrm{sim}}}{\partial\,\overline{\widetilde{u}_i\widetilde{u}_j}} = 1;\ \frac{\partial\tau_{ij}^{\Delta,\mathrm{sim}}}{\partial\overline{\bar{u}}_i} = -2\,\overline{\bar{u}}_j. \qquad (4.11b)$$

Since the only variable with uncertainty associated with it in $\overline{\widetilde{u}_i\widetilde{u}_j}$ is $\tilde{u}_i$ and $\delta\tilde{u}_i = \delta u_i$, the expression for $\delta\overline{\widetilde{u}_i\widetilde{u}_j}$ becomes:

$$\delta\overline{\widetilde{u}_i\widetilde{u}_j} = \sqrt{\left(\frac{\partial\overline{\widetilde{u}_i\widetilde{u}_j}}{\partial\tilde{u}_i}\delta u_i\right)^2}\text{, where} \qquad (4.12a)$$

$$\overline{\widetilde{u}_i\widetilde{u}_j}(\boldsymbol{x},t) = \int\left(\frac{6}{\pi\Delta^2}\right)^{3/2}\exp(-6r^2/\Delta^2)\widetilde{u}_i(x-r,t)\widetilde{u}_j(x-r,t)dr_k\text{, and} \qquad (4.12b)$$

$$\frac{\partial\overline{\widetilde{u}_i\widetilde{u}_j}}{\partial\tilde{u}_i} = 2\tilde{u}_j. \qquad (4.12c)$$

Similarly, since the only variable with uncertainty associated with it in $\overline{\bar{u}}_i$, or the double filtered velocity, is $\tilde{u}_i$ and $\delta\tilde{u}_i = \delta u_i$, the expression for $\delta\overline{\bar{u}}_i$ becomes:

$$\delta\overline{\bar{u}}_i = \sqrt{\left(\frac{\partial\overline{\bar{u}}_i}{\partial\tilde{u}_i}\delta u_i\right)^2}\text{, where} \qquad (4.13c)$$

$$\overline{\bar{u}}_i = \int\left(\frac{6}{\pi\Delta^2}\right)^{3/2}\exp(-6r^2/\Delta^2)\tilde{u}_i(x-r,t)dr_k\text{, and} \qquad (4.13b)$$

$$\frac{\partial\overline{\bar{u}}_i}{\partial\tilde{u}_i} = \int\left(\frac{6}{\pi\Delta^2}\right)^{3/2}\exp(-6r^2/\Delta^2)dr_k \qquad (4.13c)$$

Notice that the expression in Equation 4.13c is the same as Equation 4.6b for the singly filtered velocity which was determined to be 1. From this, final expression for the uncertainty associated with the SGS stress of the Similarity Model becomes:

$$\delta\tau_{ij}^{\Delta,\mathrm{sim}} = \sqrt{\left(2\tilde{u}_j\delta u_i\right)^2 + \left(-2\bar{\tilde{u}}_j\delta u_i\right)^2} \qquad (4.14)$$

The uncertainty of this modeled SGS stress as a percentage of the modeled stress for a single *Z*-slice for a single velocity field in the 33 direction, $\tau_{33}^{\Delta,\mathrm{sim}}$, can be seen in Figure 4.10.

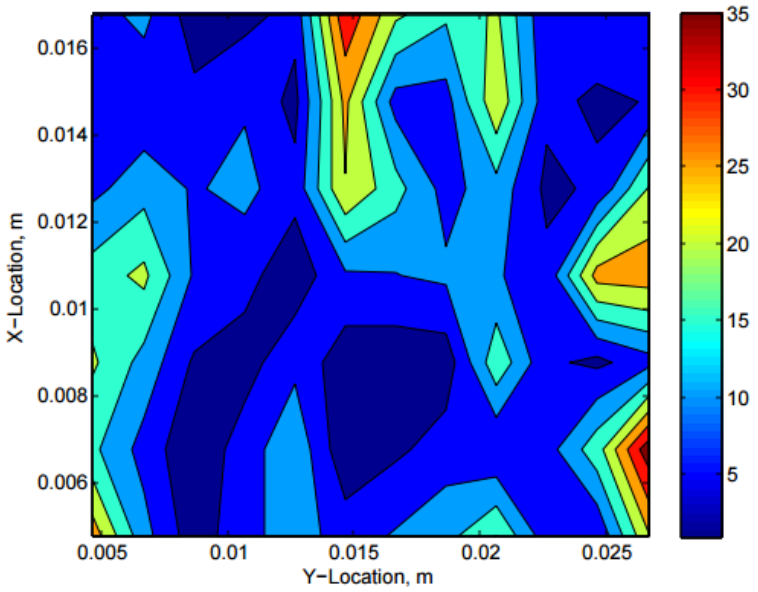


Figure 4.10: Uncertainty of $\delta\tau_{33}^{\Delta,\mathrm{sim}}$ as a percentage of $\tau_{33}^{\Delta,\mathrm{sim}}$

Notice that there are some regions of relatively high uncertainty in this slice (~30%). However, much of the uncertainty is below 15%.

The next model for to assess the uncertainty for is the mixed model. Recall that in its final form, the mixed model is given as simply the summation of the Smagorinsky and Similarity models. The resulting uncertainty is therefore simply:

$$\delta\tau_{ij}^{\Delta,\mathrm{sim}} = \sqrt{\left(\delta\tau_{ij}^{\Delta,\mathrm{sim}}\right)^2 + \left(\delta\tau_{ij}^{\Delta,\mathrm{smag}}\right)^2} \qquad (4.15)$$

The uncertainty of the Mixed Model's SGS stress a percentage of the modeled stress for a single *Z*-slice for a single velocity field in the 33 direction, $\tau_{33}^{\Delta,\mathrm{mix}}$, can be seen in Figure 4.11.

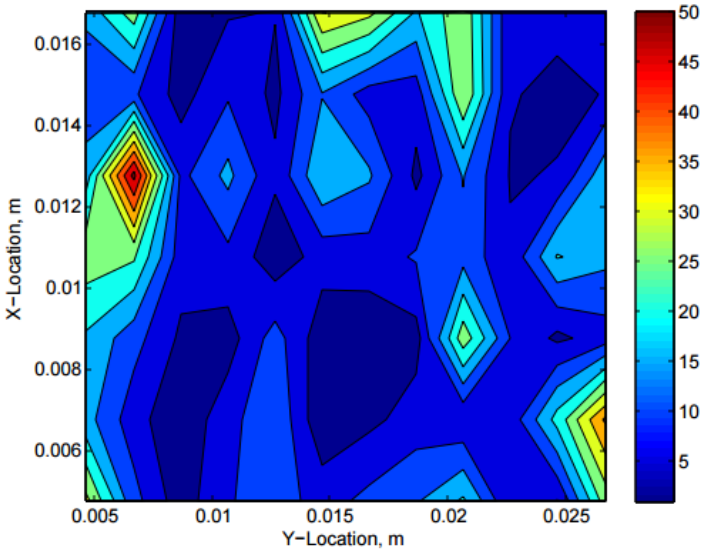


Figure 4.11: Uncertainty of $\delta\tau_{33}^{\Delta,\mathrm{mix}}$ as a percentage of $\tau_{33}^{\Delta,\mathrm{mix}}$

Notice in that there are some regions of relatively high uncertainty (~50%), but the majority of the *Z*-slice shows uncertainty values below approximately 20%. Note that, just as with the uncertainty with filtered rate of strain tensor, some of these regions of high uncertainty may simply be due to a low calculated SGS stress in these regions.

Due to the complexity of the mathematics involved in determining the uncertainty for the remaining Dynamic, Coherent Structures, and Stretched Vortex Models, the uncertainty associated with these models has been left for future work.

### 4.4 Improving the Present 3DPTV System

One of the key advantages of *a priori* testing of turbulence models using experimental data versus DNS data is that it is computationally expensive to collect DNS data at high Reynolds numbers. The above results were collected at a Reynolds number of 6274 and a

Taylor-microscale Reynolds number of 130, which are both relatively modest. The following section investigates the various ways and consequences of increasing this Reynolds number.

### *4.4.1 Methods of Increasing Reynolds Number*

Increasing the Reynolds number of the backward facing step flow can be accomplished in one of three ways, as per Equation 1.1 where $Re_H = \rho u_{in}/\nu$.

1) The kinematic viscosity, $\nu = \mu/\rho$, where $\mu$ is the dynamic viscosity of the fluid and $\rho$ is the density, can be decreased. This would require using a different fluid in the experiment and could be expensive and inefficient.
2) Increase the length-scale associated with the flow. Katz and Meneveau (1994) take advantage of this by looking far downstream of a turbulent jet where the characteristic length scales are much larger than the orifice of the jet.[20] In the backward-facing step flow experiment, this would require a new test section with a larger step and could also be expensive and inefficient.
3) The simplest way of increasing the Reynolds number is to simply increase the freestream velocity. If we consider that the fluctuating component of velocity for this flow is approximately 18% of the freestream, as per Pope 2000, then increasing the freestream velocity would also increase the turbulent Reynolds number defined in Equation 3.1 where $Re_\lambda \equiv \frac{u'\lambda}{\nu}$ and $\lambda \approx \sqrt{\frac{15\nu l}{u'}}$ is used to estimate the Taylor microscale.

### *4.4.2 Implications of Increasing Reynolds Number*

Increasing the turbulent Reynolds number of the backward-facing step flow can be accomplished by simply increasing the freestream velocity, but there are several limitations to

this increase. First, as mentioned in Section 3.3.1, the maximum flow velocity for the facility is 1.0 m/s. Once again, using Pope's guidance of the fluctuating velocity being 18% of the freestream, this results in a Reynolds number based on the step height of around 28,600 and a turbulent Reynolds number of around 278. Since DNS computational time for a three dimensional velocity field roughly scales with $\left(Re_L{}^{3/4}\right)^3$, a full DNS solution for this flow would take over 300 years, indicating the necessity for experimental methods to evaluate the turbulence models. With this said, it is important to note that the turbulent and standard Reynolds numbers for work done by Katz and Meneveau ($Re_\lambda \sim 310$ and $Re_L \sim 95000$) were higher than even the maximum flow velocity for the present flow facility. This was due to a higher freestream velocity and a larger length scale for the turbulent jet that they were studying.

A second limitation to increasing the Reynolds number is the Kolmogorov scale's sensitivity to Reynolds number. The Kolmogorov scale, or the scale associated with the smallest turbulent motions in the flow, as defined in Equation 3.2 scale with the fluctuating velocity as $\eta \sim (1/u'^3)^{1/4}$. This means that increasing the Reynolds number by increasing the freestream velocity significantly decreases the Kolmogorov scale. If the flow velocity were increased to 1 m/s in the present study, this would result in a Kolmogorov scale of approximately 47$\mu$m, about 100$\mu$m smaller than the Kolmogorov scale for the present flow settings. To accurately assess LES turbulence models, Pope 2000 recommends that the resolution be 2.1 times the Kolmogorov scale.[4] This means that the present 3DPTV system would need to be capable of resolving the flow at approximately 100$\mu$m. The 3DPTV system's maximum resolution is primarily a function of the system's magnification, imaged particle size, VOI size, and CCD resolution. Before any interpolation, the present system using $TiO_2$ particles which have an imaged diameter of 7 pixels is capable of resolving a minimum scale of approximately 145$\mu$m. This is clearly not adequate

for the 100$\mu$m scale required for the 1 m/s flow setting. In the current configuration, the maximum Reynolds number attainable based on this limitation is around 17,000 corresponding to a freestream velocity of approximately 0.59 m/s, or just over half of the tunnel's full capability. This flow setting results in a Kolmogorov scale of approximately 70$\mu$m and thus a required resolution of approximately 145$\mu$m.

### *4.4.3 CCD Resolution Study*

As previously mentioned, the maximum resolution of the 3DPTV system is dictated by the system's magnification, imaged particle size, VOI size, and CCD resolution. Perhaps the simplest and most obvious way to increase the system resolution would be to increase the resolution of the CCD or changing what type of particles were used. Dona (2015) conducted tests for an array of different particles and determined that the present $TiO_2$ <5$\mu$m particles are best suited for the system; therefore, the present study looks at how adjusting CCD resolution can change the maximum resolvable scale, and hence the maximum Reynolds number of the system.

The smallest resolvable scale various CCD resolutions was determined by first determining the total number of pixels available on the CCD and using the physical dimensions of the VOI to determine the physical spacing of the particles. This physical spacing was determined by assuming a 7 pixel diameter of the particles and taking into account a minimum particle spacing of 5 pixels. The results of this study for several different CCD resolutions capable of attaining with today's CCD technology are presented in Table 4.4:

Table 4.4: Resolvable scales for various CCD resolutions

| CCD Resolution | Max particles/image | Resolvable scale ($\mu$m) | Kolmogorov Scale ($\mu$m) | $Re_\lambda$ | $Re_H$ |
|---|---|---|---|---|---|
| 4008x2672 | 118663 | 144 | 69 | 214 | 17,000 |
| 4000x4000 | 177285 | 118 | 56 | 248 | 22,850 |
| 6000x6000 | 398892 | 79 | 38 | 321 | 38,250 |
| 8000x8000 | 709141 | 59 | 28 | 394 | 57,500 |

Notice, once again, that the maximum allowable resolution for the present 4008x2672 CCD resolution is 144$\mu$m resulting in a maximum turbulent Reynolds number of 214. The 3-dimensional PIV work done by Katz and Meneveau was accomplished on a flow with a turbulent Reynolds number of around 260.[23] If the present 3DPTV system was outfitted with a 6000x6000 (36 MP) CCD, then a turbulent Reynolds number that is 23% higher than that studied in KM is achievable. If the system were outfitted with an 8000x8000 (64 MP) CCD, then a 51% higher turbulent Reynolds number is attainable. For this reason, the most important alteration to the present 3DPTV system would be increasing the CCD resolution.

Increasing the CCD resolution allows for denser packing of particles in the flow. With this, it is important to not exceed the multiphase flow limit where the presence of the particles may impact the fluid flow rather than the flow merely impacting the velocity of the particles. A map showing the multiphase coupling regions can be seen in Figure 4.12.

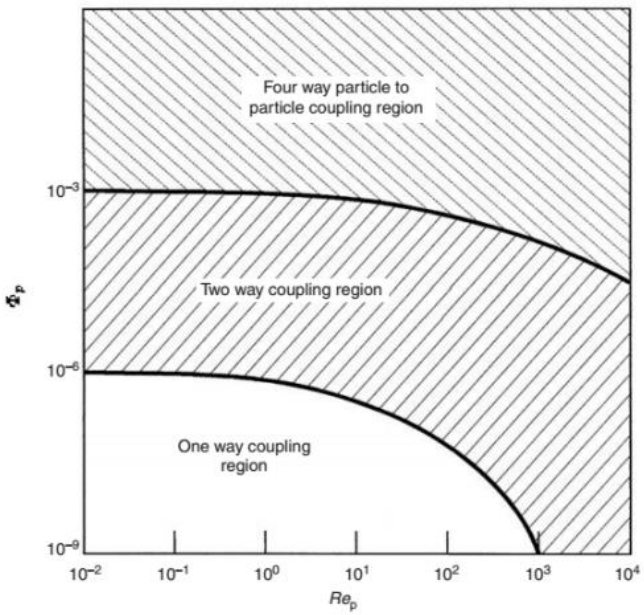


Figure 4.12: Map of multiphase coupling regions.[34]

In this map, $\Phi_P$ is the volume fraction as defined by $\Phi_P = \frac{NV_P}{V - NV_P}$ where $N$ is the number of particles in the fluid volume, $V_P$ is the volume of an individual particle, and $V$ is the size of the volume. Additionally, $Re_p$ is the particle Reynolds number given by $Re_p = \frac{\rho_f |U_f - U_P| d_p}{\mu_g}$ where $\rho_f$, $U_f$, and $\mu_g$ are the density, velocity, and viscosity of the fluid while $U_P$ and $d_p$ are the velocity and diameter of a representative particle. In the present study, the volume fraction was approximately 33.6 particles/mm$^3$ and the particle Reynolds number was trivially small as the Stokes number was small enough to say that $|U_f - U_P|$ is trivially small.[3] This places the present study well within the multiphase flow limit, but as the CCD resolution increases and it is possible to resolve more particles in a smaller volume, the cameras are capable of resolving in the two way coupling region. This must be taken into consideration when increasing CCD resolution and can be alleviated by decreasing the particle diameter, and thus the volume fraction of the particles.

*4.4.4 Improving Velocity Vector Density*

Another important improvement to the system is increasing the velocity vector field density. As noted in Section 4.1, the total vector count in the 3DPTV system's unstructured vector field ranged from 20,000 to 25,000. This count was then increased to around 65,000 vectors when the a Singular Value Decomposition (SVD) interpolation scheme was implemented by Dona.[3] In the present study, an attempt to increase this vector density was accomplished by modifying the particle siphon system.

In Dona (2015), a solution of 0.75-1.25g of $TiO_2$ powder in 0.25L of water was siphoned from a single seeding bottle into the flow at one location upstream of the test section.[3] In the present study, three solutions of 1g of $TiO_2$ powder in 0.25L of water were siphoned from three seeding bottles at three different locations upstream of the test section. For details of this siphoning system see Section 3.3.3. The increase in seeding locations led to an increase in particle density from approximately 25,000 identified particles per image to as many as 40,000 identified particles per image. An example of a full particle image in Dona (2015) is compared to a particle image from the present study in Figures 4.13 and 4.14:

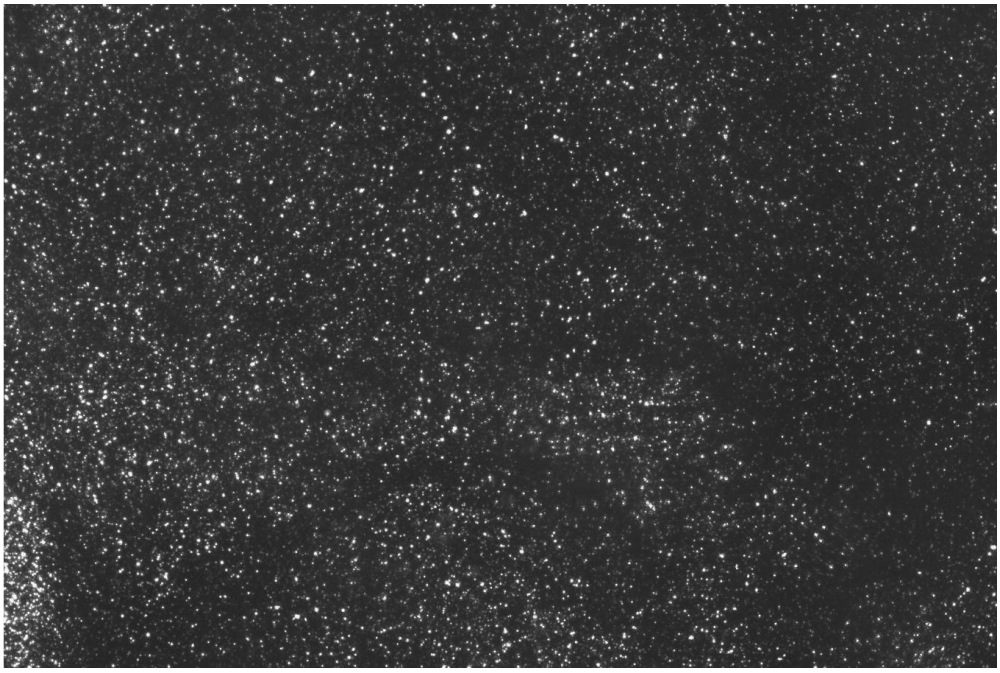

Figure 4.13: Sample particle image used to generate velocity fields in Dona (2015)[3]

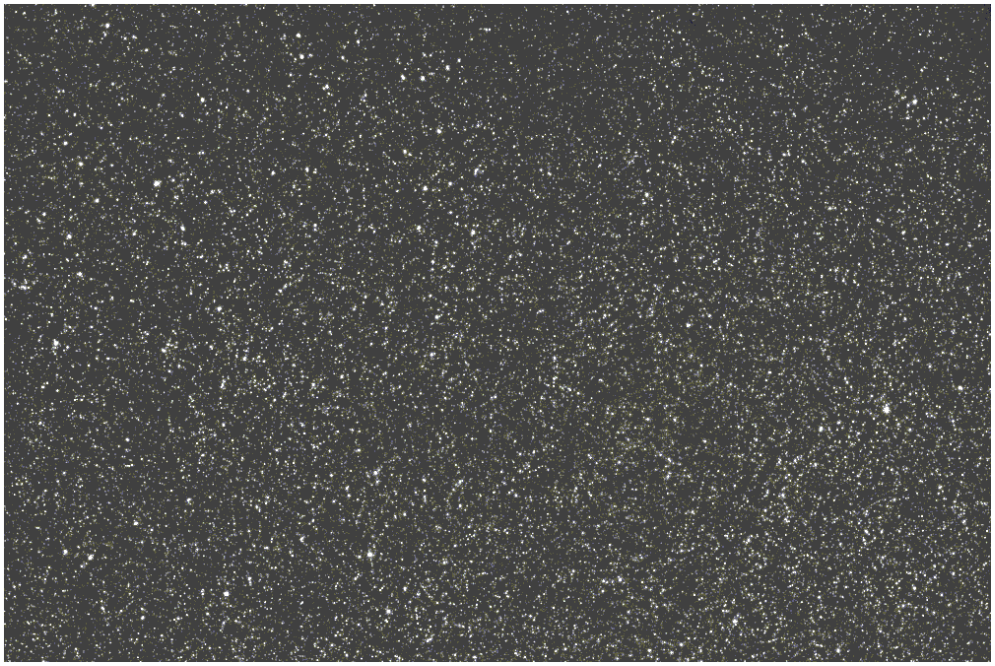

Figure 4.14: Sample particle image obtained by using new siphon approach

In these figures, notice that the new siphon system is capable of generating not only a higher density image, but also a more uniform dispersion.

# Chapter 5

# CONCLUSIONS AND FUTURE STUDY

While the present study did not produce additional 3D3C velocity vector fields beyond Dona (2015), the study did yield several key conclusions and recommendations for the improvement and design of the three-dimensional particle tracking system. The primary lessons to be taken from the present study were how to improve the imaged particle density and the analysis conducted on ways to increase the flow's Reynolds number given the present flow facility. This final chapter summarizes the work of this study and provides recommendations for future studies.

## 5.1 Conclusions

In this study, the development and implementation of a three-dimensional particle tracking (3DPTV) system was investigated and summarized. The system is based on the triangulation method of particle location and utilizes three 4008 x 2672 CCD cameras mounted on 6-axis translation stages. Three separate lenses fixed to a lens mount were used to focus the light on these CCDs and a water-filled prism was used to account for the ray bending at the interface between the water, acrylic top, and air. The tracer particles used were $<5\mu$m $TiO_2$ and were illuminated using a 532 nm Nd:YAG dual pulsed laser. The flow facility used was a dual-pump 6" x 12" water tunnel fitted with a backward-facing step test section. This flow geometry was chosen due to its consistency in separation and unsteady flow characteristics. This system

followed the same approach taken by Tien *et al.* (2014), was originally designed by Grothe (2008), and initially implemented by Dona (2015).[3,22,35]

Before collecting data to produce 3D3C velocity fields, it was necessary to calibrate the 3DPTV system. The calibration process was altered from Dona (2015) and included the use of two calibration rigs. One rig was fixed to the camera system and allowed for the removal of image distortions and the location of the system's optical axis and the other could be translated through the volume of interest for building calibration data. The data collection process was also altered from Dona (2015) by adding additional particle seeding locations. This resulted in image pairs with much higher particle density, allowing for a higher density 3D3C velocity vector field.

While a method for developing higher density velocity fields was advanced in the present study, full, accurate 3D3C velocity fields were not obtained due to CCD damage. For this reason, the lower density velocity fields developed in Dona (2015) were used in *a priori* testing of a variety of LES turbulence models. These models included the Smagorinsky, Similarity, Mixed, Dynamic, Coherent Structures, and Stretched Vortex Models. Correlation coefficients for these models achieved reasonably expected results with the exception of the Stretched Vortex Model which achieved much lower correlation coefficients than expected. A complete uncertainty analysis of the propagation of position and displacement error through these models was also accomplished, and it was determined that these two errors had negligible impacts on the accuracy of the LES results.

## 5.2 Future Study

In the process of assembling and altering the 3DPTV system, several areas of improvement became evident. These areas are listed in the sections below as recommendations for future study.

### *5.2.1 Increased CCD Resolution for Increased Reynolds Number*

Since the key advantage to using experimental data for *a priori* testing of turbulence models is the ability for experiments to resolve much higher Reynolds number flows than Direct Numerical Simulation, it is imperative that the 3DPTV system be capable of resolving high Reynolds number flows. Without changing the geometry of the flow facility used, the best way to do this would be to increase the mean flow velocity studied. The implications of doing this are investigated more fully in Section 4.1.2 and 4.3.3, but ultimately increasing Reynolds number decreases the length-scale that must be resolved. Because of this, a simple way to increase the maximum Reynolds number for the system would be to replace the 4008x2672 CCDs with new, higher resolution CCDs.

### *5.2.2 Removable Lens System for Increasing Resolution*

Another method for increasing the system's resolution and thus increasing the maximum Reynolds number for the system would be to adjust the magnification of the lenses used. This method has not been fully investigated, but would involve capturing image pairs at multiple instances of the flow. A lower magnification lens would be used first to resolve the coarse scales of the flow, then the lenses would be systematically replaced with increased magnification lenses

until a scale of $\delta = 2.1\eta$ is achieved. These sequential data sets would overlap slightly as a function of scale and then be superimposed to achieve a complete spectrum of the flow.

### *5.2.3 Smaller Particles for Increased Vector Density*

Increasing the CCD resolution as suggested in Section 5.2.1 would allow the system to resolve much smaller length-scales, but doing this would require increasing the particle seeding density. That is, to resolve the flow at a smaller scale, more particles would need to be injected into the same or smaller volume. This quickly increases the volume fraction of the flow and can result in multi-phase flow effects, as discussed in Section 4.4.3. One way to avoid these multi-phase flow effects would be to decrease the particle Reynolds number, $Re_p$, by decreasing the particle diameter. This decrease in particle diameter could significantly increase vector density.

### *5.2.4 Re-evaluation of the Calibration Method*

While the present calibration method is adequate and capable of yielding low uncertainty velocity fields, the process is incredibly sensitive to disturbance, time consuming, and significant improvement should be made to the hardware used. The present calibration process requires two separate calibration rigs. One rig is attached to the optical/camera assembly while the other rests on the top of the flow facility. While this is capable of producing accurate calibration data, it is recommended that these two rigs be combined into one rig that attaches directly to the camera assembly and is capable of translating through the volume of interest. For accurate 3DPTV results, distortions of the camera-fixed calibration rig must be removed when it is centered on the optical axis of the system. This means that when the translation rig is used, any distortions that appear cannot be removed by adjusting CCD location or angle, but since the calibration software

requires that distortions on this rig also be removed, it is necessary to remove the distortions of this rig manually. This is incredibly difficult as distortions result from very small movement of the rig. A combined rig would allow for removal of distortion and translation through the VOI in one step and would greatly streamline the calibration process.

### *5.2.5 Re-evaluation of the Camera Setup*

In its present configuration, the 3DPTV system is mounted on a scaffolding frame that is separate from the flow facility. This necessitates the tedious alignment of two large systems which inherently contains some level of uncertainty and error that could propagate to the final accuracy of the 3D3C velocity fields. For this reason, it is suggested that each camera/lens be mounted as a single system (unlike the DDPIV system), and that each camera/lens be mounted around the test section so as to surround the volume of interest in a true triangulation imaging system. This would also aid in the present calibration procedure by ensuring that both rigs are aligned to the same reference. One method of accomplishing this would be to add rails to the water tunnel and fixing wheels or struts to the bottom of the camera/optical system thus allowing the system to be translated along the tunnel while remaining centered over the test section's centerline. The system would look similar to that used in Maas *et al.* (1995) as shown in Figure 5.1.

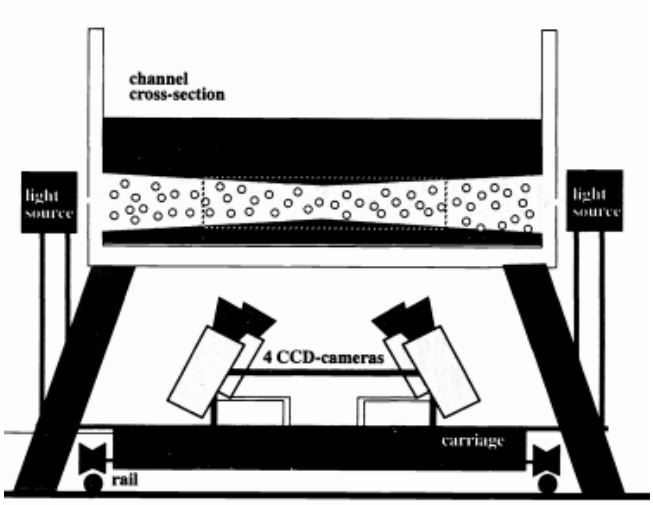


Figure 5.1: Example configuration for new 3DPTV system[36]

*5.2.6 Additional Evaluation of Stretched Vortex Model*

The poorest performing LES model in this study was the Stretched Vortex Model, SVM. This is surprising, especially due to the vortical nature of backward-facing step flow. The version of the SVM used, as presented in Section 2.3.8, was the basic SVM and more complex versions of the model exist.[18] Specifically, some of these models involve aligning the sub-grid vortex axes with a weighted combination of the strain rate eigenvector and the vorticity vector. A more thorough investigation of how this weighting affects the overall correlation coefficients for the SVM should be investigated. Additional validation of the code via analytic functions with turbulent characteristics.

*5.2.7 Further Recommendations from Dona*

In addition to the above recommendations for future study, there were several important recommendations in Dona (2015) that were not able to be completed in the present study and are worth investigating. For completeness, these are listed below as given in Dona (2015).

1. The interpolation scheme used in Dona's data to increase vector density should be fully assessed using the techniques developed and described by Talapatra and Katz 2012.[31] Dona suggests that this test be performed iteratively in conjunction with the 3-D unstructured median outlier filtering technique to achieve the most accurate, highest-density, divergence-free interpolation with the fewest outliers.[3]
2. Further analysis of the 3DPTV tracking algorithm is suggested. This includes the effect of an iterative $\sigma$, or Gaussian mask size, definition (see Chapter 4 of Dona for details) on the accuracy of tracking results.[3]
3. An investigation into processing techniques such as a Proper Orthogonal and Dynamic Mode Decomposition as employed by Sampath and Chakravarthy (2014) on the 3DPTV tracking algorithm is suggested.[37]
4. Further analysis of the impact of the image processing, de-noising, and contrast adjustment steps in the 3DPTV tracking algorithm is suggested. For additional detail on the 3DPTV tracking algorithm, see Dona (2015).[3]

### *5.2.8 Ranking of Future Studies*

While each of the suggestions for future study serve to advance the 3DPTV system, some of the future recommendations are more imperative than others. These high priority recommendations are listed below:

1. The most important recommendation for future work is increasing the Reynold's number, and hence the Taylor-microscale Reynolds number of the flow. The most plausible way of doing this would be to increase the CCD resolution allowing for the resolution of smaller length-scales of the flow.

2. The second most important recommendation for future work is re-evaluating and re-designing the calibration process. Streamlining and simplifying this process would not only decrease the uncertainty associated with the experiment, but would also allow for the execution of more experiments, perhaps at varying Reynolds numbers or with different tracer particles.
3. The third most important recommendation is re-evaluating and redesigning the camera setup. In its present configuration, the setup is difficult to work with and contains inherent uncertainty. In the author's opinion, accomplishing these three recommendations would not only greatly improve confidence in the accuracy of the results, but would also significantly streamline the data collection process and result in more velocity fields for *a priori* testing.

# BIBLIOGRAPHY

[1] D. Vergano. Turbulence theory gets a bit choppy. *USA Today*. September, 2006.

[2] P. G. Spazzini, G. Iuso, M. Onorato, N. Zurlo, and G. M. Di Cicca. Unsteady behavior of back-facing step flow. *Experiments in Fluids*, 30(5):551561, May 2001.

[3] N. Dona. Implementation of 3DPTV for turbulence analysis and subgrid-scale stress model testing of a backward-facing step flow. Master's thesis, University of Washington, 2015.

[4] S. B. Pope. *Turbulent Flows*. Cambridge University Press, 2000.

[5] T. R. Troutt, B. Scheelke, and T. R. Norman. Organized structures in a reattaching separated flow field. *J. Fluid Mech*., 143(-1):413, Jun 1984.

[6] F. Scarano, C. Benocci, and M. L. Riethmuller. Pattern recognition analysis of the turbulent flow past a backward facing step. *Physics of Fluids*, 11(12):3808, 1999.

[7] C. Meneveau and J Katz. Scale-invariance and turbulence models for large-eddy simulation. *Annu. Rev. Fluid Mech*., 2000.

[8] B F Armaly, F Durst, J C F Pereira, and B Schonung. Experimental and theoretical investigation of backward-facing step flow. *J. Fluid Mech*., 1983.

[9] M. Barri, G. K. El Khoury, H. I. Andersson, and B. Pettersen. DNS of backward-facing step flow with fully turbulent inflow. *International Journal for Numerical Methods in Fluids*, page n/an/a, 2009.

[10] P. M. Nadge and R. N. Govardhan. High reynolds number flow over a backward-facing step: structure of the mean separation bubble. *Experiments in Fluids*, 55(1), Jan 2014.

[11] T. Kobayashi, Y. Morinishi, and K. Oh. Large eddy simulation of backward-facing step flow. *Communications in Applied Numerical Methods*, 8(7):431441, Jul 1992.

[12] A. Leonard. Energy cascade in large-eddy simulations of turbulent fluid flows. *Turbulent Diffusion in Environmental Pollution, Proceedings of a Symposium held at Charlottesville*, page 237248, 1975.

[13] J. Smagorinsky. General circulation experiments with the primitive equations. *Monthly Weather Review*, 91(3):99164, Mar 1963.

[14] J. Bardina, J. Ferziger, and W. Reynolds. Improved subgrid-scale models for large-eddy simulation. *13th Fluid and PlasmaDynamics Conference*, Jul 1980.

[15] Massimo Germano, Ugo Piomelli, Parviz Moin, and William H. Cabot. A dynamic subgrid-scale eddy viscosity model. *Phys. Fluids* A, 3(7):1760, 1991.

[16] D. K. Lilly. A proposed modification of the germano subgrid-scale closure method. *Phys. Fluids* A, 4(3):633, 1992.

[17] H. Kobayashi. The subgrid-scale models based on coherent structures for rotating homogeneous turbulence and turbulent channel flow. *Physics of Fluids*, 17(4):045104, 2005.

[18] A. Misra and D. I. Pullin. A vortex-based subgrid stress model for large-eddy simulation. *Physics of Fluids*, 9(8):2443, 1997.

[19] S. Liu, C. Meneveau, and J. Katz. Experimental study of similarity subgrid-scale models of turbulence in the far-field of a jet. *Appl. Sci. Res*., 54(3):177190, Apr 1995.

[20] S Liu, C Meneveau, and J Katz. On the properties of similarity subgrid-scale models as deduced from measurements in a turbulent jet. *J. Fluid Mech*., 1994.

[21] C. Pantano, D.I. Pullin, P.E. Dimotakis, G. Matheou. LES Approach for high Reynolds number wall-bounded flows with application to turbulent channel flow. *Journal of Computational Physics,* 227,9271–9291, 2008.

[22] R Grothe. Modification of a DDPIV system for imaging small volumes using triangulation for particle identification. Master's thesis, University of Washington, 2008.

[23] B Tao, J Katz, and C Meneveau. Statistical geometry of subgrid-scale stresses determined from holographic particle image velocimetry measurements. *J. Fluid Mech*., 2002.

[24] F Pereira, M Gharib, D Dabiri, and D Modarress. Defocusing digital particle image velocimetry: a 3-component 3-dimensional DPIV measurement technique. application to bubbly flows. *Exp. Fluids*, 2000.

[25] L. Kajitani, D. Dabiri. A full three-dimensional characterization of defocusing digital particle image velocimetry. *Measurement and Science Technology,* 16, 790-804. 2005.

[26] R. Grothe, G. Rixon, D. Dabiri. An improved three-dimensional characterization of defocusing digital particle image velocimetry (DDPIV) based on a new imaging volume definition. *Measurement and Science Technology,* 19,065402, 2008.

[27] Y.-C. Lei, W.-H. Tien, J. Duncan, M. Paul, N. Ponchaut, C. Mouton, D. Dabiri, T. Rsgen, and J. Hove. A vision-based hybrid particle tracking velocimetry (PTV) technique using a modified cascade correlation peak-finding method. Experiments in Fluids, 53(5):12511268, Aug 2012.

[28] Illunis. *Illunis XMV-11000 USA OEM Q2-04 Product Brief,* 2004.

[29] D Schmitt. Development of a 3-D defocusing liquid crystal thermometry and velocimetry (3DDLCPTV) system. Master's thesis, University of Washington, 2007.

[30] Schneider-Kreuznach. *Makro-Symmar HM.*

[31] S. Talapatra and J. Katz. Three-dimensional velocity measurements in a roughness sublayer using microscopic digital in-line holography and optical index matching. *Measurement Science and Technology,* 24(2):024004, Dec 2012.

[32] U. Piomelli, W. H. Cabot, P. Moin, and S. Lee. Subgrid-scale backscatter in turbulent and transitional flows. *Phys. Fluids* A, 3(7):1766, 1991.

[33] J. R. Taylor. *An Introduction to Error Analysis: The Study of Uncertainties in Physical Measurements.* University Science Books, 1982.

[34] C T Crowe, T R Troutt, and J N Chung. Numerical models for two-phase turbulent flows. *Annual Review of Fluid Mechanics*, 28(1):1143, Jan 1996.

[35] W H Tien. *3-D Particle Tracking Velocimetry: Development and Applications in Small Scale Flows*. PhD thesis, University of Washington, 2013.

[36] H G Maas, A Gruen. Digital photogrammetric techniques for high-resolution three-dimensioinal flow velocity measurements. *Opt Eng.* 34(7), 1970-1976. 1995.

[37] R Sampath and S. R. Chakravarthy. Proper orthogonal and dynamic mode decompositions of time-resolved piv of confined backward-facing step flow. *Experiments in Fluids*, 55(9), Aug 2014.